

Gas Phase Synthesis of the C₄₀ Nano Bowl C₄₀H₁₀

Author List

Lotefa B. Tuli,¹⁺ Shane J. Goettl,²⁺ Andrew M. Turner,² A. Hasan Howlader,^{1,3} Patrick Hemberger,^{*4} Stanislaw F. Wnuk¹, Tianjian Guo⁵, Alexander M. Mebel,^{*1} Ralf I. Kaiser^{*2}

Affiliations

¹ *Department of Chemistry and Biochemistry, Florida International University, Miami, FL 33199, USA*

² *Department of Chemistry, University of Hawai'i at Mānoa, Honolulu, HI 96822, USA*

³ *Present Address: Department of Chemistry, Johns Hopkins University, Baltimore, Maryland, 21218, USA.*

⁴ *Paul Scherrer Institute, CH-5232, Villigen PSI, Switzerland*

⁵ *School of Pharmaceutical Science and Technology, Tianjin University, 92 Weijin Road, Tianjin, 370001, PR China*

Corresponding Author Prof. Alexander M. Mebel: mebela@fiu.edu

Corresponding Author Prof. Dr. Ralf I. Kaiser: ralfk@hawaii.edu

Corresponding Author Dr. Patrick Hemberger: patrick.hemberger@psi.ch

⁺ Contributed equally to this work.

Abstract

Nanobowls represent vital molecular building blocks of end-capped nanotubes and fullerenes detected in combustion systems and in deep space such as toward the planetary nebula TC-1, but their fundamental formation mechanisms have remained elusive. By merging molecular beam experiments with electronic structure calculations, we reveal a complex chain of reactions initiated through the gas-phase preparation of benzocorannulene ($C_{24}H_{12}$) via ring annulation of the corannulenyl radical ($C_{20}H_9^{\bullet}$) by vinylacetylene (C_4H_4) as identified isomer-selectively *in situ* via photoionization efficiency curves and photoion mass-selected threshold photoelectron spectra. *In silico* studies provided compelling evidence that the benzannulation mechanism can be expanded to pentabenzocorannulene ($C_{40}H_{20}$) followed by successive cyclodehydrogenation to the C₄₀ nanobowl ($C_{40}H_{10}$) – a fundamental building block of buckminsterfullerene (C_{60}). This high-temperature pathway opens up isomer-selective routes to nanobowls via resonantly stabilized free-radical intermediates and ring annulation in circumstellar envelopes of carbon stars and planetary nebulae as their descendants eventually altering our insights of the complex chemistry of carbon in our Galaxy.

Introduction

The discovery of the fullerenes buckminsterfullerene (C_{60}) and rugbyballene (C_{70})—allotropes of carbon consisting of carbon atoms connected by single and double bonds forming closed structures with five- and six-membered rings—nearly 40 years ago by Kroto, Heath, O'Brien, Smalley, and Curl¹ has paved the path to remarkable scientific breakthroughs in material sciences, medicinal chemistry, physical chemistry, and organic chemistry². This is due to the role of fullerenes as light-activated antimicrobial agents³, contrast agents⁴, molecular electronics⁵, lubricants⁶, and surface coatings⁷. In the post-fullerene era, edge-hydrogenated fullerene clusters attracted particular attention as molecular building blocks to form fullerenes and nanotubes from the bottom up. Here, the beauty of such often highly symmetric molecules triggered extensive interest from synthetic organic chemists who attempted to isolate the clusters by slicing the geodesic domes of fullerenes and saturating the dangling bonds of edge carbon atoms by hydrogen atoms⁸⁻¹⁰. Fullerene fragments, which belong to an extended family of curved (three-dimensional) polycyclic aromatic hydrocarbons (PAHs), with the prototype species being the smallest bowl-shaped corannulene ($C_{20}H_{10}$) molecule (Fig. 1) are of special interest^{11,12}. When arranged symmetrically in the condensed phase, such nanobowls afford an array of materials supported in changeable complex environments such as intermolecular charge transports¹², which is rather distinct from the conventional mechanism based upon a tight overlap of π molecular orbitals in stacked carbonaceous materials.

Corannulene ($C_{20}H_{10}$), a stem circulene with a central polygon surrounded by six-membered aromatic rings, has been identified as the smallest bowl-shaped fragment of buckminsterfullene (C_{60}), which also possesses the C_5 rotational axis^{8,13-16}. However, the synthesis of more complex buckybowls such as C40 ($C_{40}H_{10}$) and C50 ($C_{50}H_{10}$) nanobowls¹² along with C39 ($C_{39}H_{12}$) and C46 ($C_{46}H_{12}$) nanobaskets¹⁷ has remained a fundamental synthetic challenge. Whereas the formation and isolation of these buckybowls is interesting by itself from the synthetic chemistry

viewpoint, the ultimate goal is to exploit these nanostructures as transitional templates to direct the synthesis of the closed icosahedral C₆₀–fullerene structure and to employ them as end-caps of nanotubes^{11,18,19}. Over the last decades, remarkable preparative organic synthetic routes have been reported to prepare mono- to pentabenzocorannulenes (C₄₀H₂₀) via addition of six-membered benzene rings, or benzannulation^{20,21}, to the edge of corannulene^{10,11,18,22,23} but these pathways could not rationalize the synthetic routes to naturally prepared fullerenes detected in combustion flames²⁴, in meteorites such as Allende and Murchison²⁵, and in the planetary nebula TC-1²⁶. Consequently, hitherto elusive high temperature chemical routes for the synthesis of fullerenes along with their nanobowls must exist either from the bottom up²⁷⁻²⁹ or from top-down²⁹⁻³⁵.

Here, by combining molecular beam experiments with electronic structure calculations, we report on a complex chain of reactions initiated through the gas-phase preparation of benzocorannulene (C₂₄H₁₂) via ring annulation of the corannulenyl radical (C₂₀H₉•) by vinylacetylene (C₄H₄) as identified isomer-selectively *in situ* via fragment-free photoionization extracting photoionization efficiency curves (PIE) and photoion mass-selected threshold photoelectron spectra (ms-TPES). Exploiting benzocorannulene (C₂₄H₁₂) as a benchmark, we further expose *in silico* that the benzannulation mechanism can be expanded up to pentabenzocorannulene (C₄₀H₂₀) (Fig. 2), which encompasses two thirds of the carbon content of C₆₀, followed by successive cyclodehydrogenation to the C₄₀ nanobowl (C₄₀H₁₀)³⁶. In turn, the latter exhibits with a deep bowl geometry and has curvature similar to that of buckminsterfullerene. The exploitation of linearly scaling coupled cluster method for electronic structure calculations of molecules as large as C₄₀H₂₀ opens a previously unavailable avenue for accurate exploration of potential energy diagrams of complex molecules with chemical accuracy allowing to obtain detailed information on energies of metastable states/products, barriers, and chemical pathways complementary to experimental data. This high-temperature route opens up a facile, isomer-selective bottom up pathway to nanobowls via resonantly stabilized free-radical intermediates and

ring annulation in combustion flames and in planetary nebulae, which may act as precursors to buckminsterfullerene (C_{60}) thus changing our conception of the formation of complex carbon nanostructures in our Galaxy.

Results

Mass Spectra. A representative mass spectrum recorded at a photon energy of 9.00 eV for the reaction of corannulenyl radicals ($C_{20}H_9^{\bullet}$) with vinylacetylene (C_4H_4) is shown in Fig. 3b, while the mass spectrum for the reference experiment of bromocorannulene ($C_{20}H_9Br$) seeded in helium (He) without vinylacetylene is shown in Fig. 3a. In both systems, prominent ion counts were observed at $m/z = 328$ ($C_{20}H_9^{79}Br^+$) and 330 ($C_{20}H_9^{81}Br^+$). These signals correspond to the ^{79}Br and ^{81}Br isotopes of the bromocorannulene precursor, respectively. Under pyrolysis conditions in the presence of vinylacetylene (Fig. 3b), additional peaks arose at $m/z = 249, 250, 251, 274, 300,$ and 301. The former two can be assigned to the molecular formulas $C_{20}H_9^{+\bullet}$ and $C_{20}H_{10}^+$ indicating the corannulenyl radical formed via pyrolysis of bromocorannulene and corannulene generated through hydrogen abstraction and/or addition of atomic hydrogen, respectively. Signal at $m/z = 251$ can be connected to ^{13}C -substituted corannulene, whereas ion counts at $m/z = 274$ likely originate from the reaction of corannulenyl ($C_{20}H_9^{\bullet}$; 249 amu) with acetylene (C_2H_2 ; 26 amu; impurity from the vinylacetylene cylinder) resulting in $C_{22}H_{10}$ isomer(s) attributed to 2-ethynylcorannulene and/or cyclopenta[*c,d*]corannulene. Finally, these data provide evidence that peaks at $m/z = 300$ and 301 are associated with the corannulenyl ($C_{20}H_9^{\bullet}$; 249 amu)–vinylacetylene (C_4H_4 ; 52 amu) reaction resulting in the formation of $C_{24}H_{12}$ isomer(s) and their ^{13}C -substituted counterpart(s).

Results

PIE Curves. Having assigned a hydrocarbon molecule(s) with the molecular formula $C_{24}H_{12}$ formed from the reaction of the corannulenyl radical with vinylacetylene, the structural isomer(s) must now be identified. This is accomplished by thoroughly analyzing the corresponding photoionization efficiency (PIE) curve and ms-TPES of $m/z = 300$ ($C_{24}H_{12}^+$), which are presented in Fig. 4a and Fig. 5 along with reference spectra. Let us focus on the PIE curve first. The experimentally derived PIE curve at $m/z = 300$ (black) reproduces the reference PIE curve of the benzocorannulene (red) sample above 7.70 eV very well (Fig. 4a). However, the ionization onset for the experimental curve of 7.45 ± 0.05 eV ($m/z = 300$) and 7.40 ± 0.05 eV ($m/z = 301$) does not match the onset of 7.70 ± 0.05 eV for the benzocorannulene curve. This may indicate that additional species beyond benzocorannulene are present in the molecular beam. Alternative isomers 4-(1-buten-3-yne)corannulene and 4-(3-buten-1-yne)corannulene have calculated adiabatic ionization energies of at 7.54 ± 0.05 eV and 7.53 ± 0.05 eV, respectively (Fig. 4a). The onset for these isomers lies below that of benzocorannulene (7.70 eV); therefore, 4-(1-buten-3-yne)corannulene and 4-(3-buten-1-yne)corannulene may contribute to signal intensity of the experimental PIE curve below 7.7 eV to about 7.5 eV. The remaining intensity of the experimental PIE curve below 7.5 eV exhibits a gradual rise from zero indicative of hot bands³⁷. Consequently, signal from about 7.4 to 7.7 eV arises from hot bands and/or from the 4-(1-buten-3-yne)corannulene and 4-(3-buten-1-yne)corannulene isomers, while a comparison of the corannulenyl–vinylacetylene and benzocorannulene PIE curves indicates that up to 99 % of the total ion counts of the corannulenyl–vinylacetylene curve at photon energies beyond 7.7 eV can be attributed to benzocorannulene. It is important to note that the PIE curve taken at $m/z = 301$ (Fig. 4b) is essentially superimposable on the $m/z = 300$ (Fig. 4a) curve after scaling (Supplementary Fig. 2). Consequently, the data at $m/z = 301$ can be attributed to ^{13}C -substituted isomers ($^{13}CC_{23}H_{12}$) of benzocorannulene at an abundance of about 26 % to account for the 1.1 % natural abundance of

¹³C. Therefore, our results on the PIE curves reveal the formation of benzocorannulene through the reaction of the corannulenyl radical with vinylacetylene.

Results

ms-TPE Spectra. In addition, we validated our assignment by exploiting the ms-TPES data (Fig. 5). The ms-TPE spectra for the corannulenyl–vinylacetylene system (black) and benzocorannulene (blue) reference spectrum show clear structure and, like the PIE curves, expose an excellent overlap from about 7.7 eV to 9.0 eV; this experimental evidence reinforces our conclusion that the major product of the corannulenyl–vinylacetylene reaction is indeed benzocorannulene. Besides this experimental evidence, we provided further computational evidence on the formation of benzocorannulene. The calculated Franck-Condon (FC) factors for benzocorannulene (red), 4-(1-buten-3-yne)corannulene (green), and 4-(3-buten-1-yne)corannulene (orange) are shown as stick spectra in Fig. 5, while calculated ionization energies of 8.15, 8.18, and 8.45 eV for the $2^2A''$, $1^2A'$, and $3^2A''$ excited electronic states of the benzocorannulene cation are denoted by dashed vertical lines (magenta). Especially the $2^2A''$ and $1^2A'$ states are responsible for the broad band centered at around 8 eV in both the reference and experimental ms-TPE spectra. The origin transition of the benzocorannulene FC spectrum at 7.65 ± 0.10 matches the ionization onset of the benzocorannulene ms-TPE and PIE spectra. The bands between 8.0 and 8.5 eV of the ms-TPES are comprised of up to three excited states, which may prevent the visibility of the true ionization onset. All states have vibrational transitions, which may overlap leading to the broad features. The 4-(1-buten-3-yne)corannulene and 4-(3-buten-1-yne)corannulene FC spectra show intense transitions at 7.56 ± 0.05 and 7.55 ± 0.05 , respectively, indicating that these isomers may account for some of the intensity of the experimental spectrum below the onset of benzocorannulene, while the signal below 7.5 eV is due to hot band transitions. Overall, combining the PIE curves and ms-TPE spectra analyses provides compelling evidence for the formation of at least benzocorannulene

from the reaction of corannulenyl radicals with vinylacetylene. It shall be highlighted that the combined extraction of PIE and ms-TPES data represents an authenticated approach to identify complex organic molecules as demonstrated at state-of-the-art VUV beamlines at Soleil (France)³⁸⁻⁴⁰, the Swiss Light Source (Switzerland)⁴¹⁻⁴³, and the Advanced Light Source (US)^{44,45}.

Discussion

We are exploiting now linearly scaling coupled cluster electronic structure calculations to explore the complex reactions leading ultimately to the gas phase formation of the C₄₀ nanobowl (C₄₀H₁₀). This is accomplished in three steps. First, having identified benzocorannulene (C₂₄H₁₂), we unravel the mechanism of the gas phase formation of benzocorannulene. This reaction sequence serves as a prototype to benchmark the experimental findings with linearly scaling coupled cluster methods. Second, these computations are expanded to pentabenzocorannulene (C₄₀H₂₀) via successive benzannulations. Finally, five successive ring-closures are explored computationally to eventually prepare the C₄₀ nanobowl (C₄₀H₁₀).

The corannulenyl radical (C₂₀H₉[•]) first forms a van-der-Waals complex **i1** with vinylacetylene (C₄H₄) stabilized by 4.7 kJ mol⁻¹ (Fig. 6). In order to form a covalent C-C bond between the vinylic terminal CH₂ moiety and the radical site in C₂₀H₉[•], the system needs to overcome a small barrier of 0.2 kJ mol⁻¹ with respect to **i1**; the corresponding transition state is submerged with respect to the initial reactants since it resides 4.5 kJ mol⁻¹ below their energy level thus resulting in an effective barrierless formation of **i2** via C-C bond formation. This intermediate can eventually undergo ring annulation and hydrogen atom loss resulting in benzocorannulene (**p1**). In detail, this process involves migration of the hydrogen atom from the *ortho* position in the attacked aromatic ring in **i2** to the β carbon atom in the side chain (**i2** \rightarrow **i3**), a facile six-membered ring closure (**i3** \rightarrow **i4**) via a barrier of only 10 kJ mol⁻¹, a hydrogen atom shift in the newly formed six-membered ring from a CH₂ group to the neighboring bare carbon atom (**i4** \rightarrow **i5**), and elimination of a hydrogen

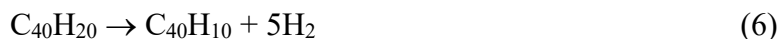
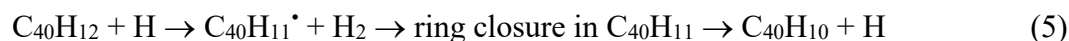
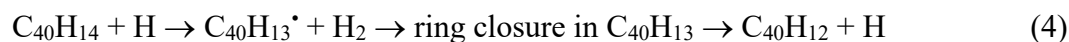
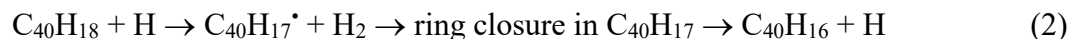
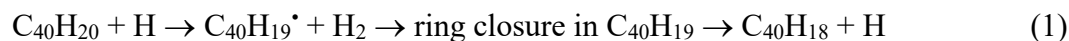
atom from the remaining CH₂ group accompanied by aromatization to **p1**. Several pathways to side-chained C₂₄H₁₂ isomers exist, but at 10 K these reactions are not competitive with the exoergic formation of benzocorannulene (C₂₄H₁₂) (−292 kJ mol^{−1}) (Supplementary Fig. 6). Overall, as supported by kinetics calculations as detailed in Supplementary Note 4, the barrierless reaction to benzocorannulene represents a facile pathway even at temperatures of 10 K in cold molecular clouds; at elevated temperatures, **p1** is formed predominantly via hydrogen assisted isomerization of the side-chained isomers 4-(1-buten-3-yne)corannulene and 4-(3-buten-1-yne)corannulene (Supplementary Fig. 8).

The experimental and theoretical results unambiguously demonstrate a facile formation of benzocorannulene (C₂₄H₁₂). Therefore, analogous benzannulation routes are feasible from benzocorannulene to pentabenzocorannulene (Fig. 2), where the ring annulation sequentially occurs on all five outside six-membered rings of the initial corannulene molecule. Note that in cold molecular clouds at 10 K, hydrogen abstraction reactions activating closed-shell species to radicals prior to their reactions with vinylacetylene are closed due to the inherent barriers of abstraction; however, the ultraviolet photon field present even deep inside cold molecular clouds and around planetary nebulae can photolyze corannulene leading via carbon-hydrogen bond rupture to the corannulenyl radical plus atomic hydrogen. Since the hydrogen abstraction and specifically vinylacetylene addition reactions proceed through benzannulation⁴⁶ (Supplementary Table 1), here we focus on the potential energy diagram for the tetrabenzocorannulenyl radical (C₃₆H₁₇·) plus vinylacetylene (C₄H₄) reaction, i.e. the final ring annulation pathway (Fig. 7). The reactants can form a van der Waals complex **i6** stabilized by 3.4 kJ mol^{−1}. Next, the formation of the covalently bound intermediate **i7** proceeds via a 6.7 kJ mol^{−1} barrier; this barrier is not submerged as the corresponding transition state resides 3.3 kJ mol^{−1} above the reactants' zero energy level. The latter undergoes a hydrogen shift to **i8** followed by the six-membered ring closure to **i9**, a hydrogen migration to **i10**, and finally, hydrogen atom elimination to pentabenzocorannulene (C₄₀H₁₂, **p2**).

The critical transition state on the pathway from **i7** to **p2** is the first hydrogen shift step with the transition state located 37 kJ mol⁻¹ lower in energy than the separated reactants. This position is 7 kJ mol⁻¹ higher than that for the corresponding **i2**→**i3** transition state in the reaction of the [C₂₀H₉][•] radical with vinylacetylene (Fig. 6). Also, the overall reaction exoergicity to produce **p2** decreases to 245 kJ mol⁻¹ from 292 kJ mol⁻¹ for the formation of **p1** and generally, the relative energies of the intermediates and transition states on the ring annulation pathway in the [C₃₆H₁₇][•] plus vinylacetylene reaction increase by up to 35–47 kJ mol⁻¹ compared to [C₂₀H₉][•] plus vinylacetylene. This is also the case for the formation of **p3**, where the relative energies of the hydrogen loss transition state from **i7** and the product increase to 1 kJ mol⁻¹ above and 7 kJ mol⁻¹ below the reactants' level.

Pentabenzocorannulene is chiral, as are the intermediate di-, tri-, and tetrabenzocorannulenes all containing at least one [4]-helicene moiety in their structures. As illustrated in Fig. 8, pentabenzocorannulene contains five overlapping [4]-helicene units in its structure. Interestingly, the in-between vinylacetylene addition reactions do not have to have positive entrance barriers; we anticipate that the barriers remain submerged if hydrogen atom abstraction preceding vinylacetylene addition takes place at a zigzag edge but would be positive if hydrogen abstraction happens on an armchair edge of the intermediate benzocorannulenes. In addition, there is a multitude of different pathways from benzocorannulene to tetrabenzocorannulene depending on which hydrogen atom is abstracted at each stage (Fig. 2). According to the computed rate constants for the [C₃₆H₁₇][•] plus vinylacetylene reaction (Supplementary Fig. 8(c)), its kinetics are analogous to those of [C₂₀H₉][•] plus vinylacetylene. At the conditions relevant to combustion flames or circumstellar envelopes, the primary reaction would mostly form the side chain C₄₀H₂₀ isomers like **p3**, but their secondary, hydrogen-assisted isomerization would efficiently convert them into the much more thermodynamically favorable **p2**.

Finally, we consider the fate of **p2** at high temperature conditions in the presence of radicals, which can abstract hydrogen atoms, or of a strong vacuum ultraviolet photon field in deep space, which cleave the carbon-hydrogen bond. **p2** possesses five bay areas, which may undergo a five-membered ring closure following a hydrogen loss reaction either through hydrogen abstraction or photolysis. Thus, five consecutive hydrogen abstraction – five-membered ring closure – hydrogen atom loss (cyclodehydrogenation) processes may potentially lead to the C40 nanobowl (C₄₀H₁₀) (Fig. 9 and Supplementary Fig. 10) as shown in equations 1–6.



The hydrogen abstraction barrier for C₄₀H₂₀ (71 kJ mol⁻¹) is close to a typical value for the hydrogen abstraction reaction from an armchair PAH edge (69 kJ mol⁻¹) and compares to 68 kJ mol⁻¹ for a zigzag edge and 67 kJ mol⁻¹ for benzene and naphthalene⁴⁷; the hydrogen atom abstraction barriers remain in the narrow range of 69-75 kJ mol⁻¹ for the complete reaction sequence (Supplementary Fig. 10). The hydrogen abstraction reaction to [C₄₀H₁₉][•] (**i11**) is 21 kJ mol⁻¹ endoergic, which is lower than the typical endoergicity of 30 kJ mol⁻¹ for such a reaction from an armchair edge of a PAH. At the next step, **i11** undergoes a five-membered ring closure at the affected bay area producing **i12**. This reaction stage is completed by a loss of the extra hydrogen from the newly created five-membered ring overcoming a 141 kJ mol⁻¹ barrier and forming C₄₀H₁₈ (**p4**). The two-step unimolecular decomposition of **i11** via atomic hydrogen loss to **p4** is overall 108 kJ mol⁻¹ endoergic and requires the highest barrier of 130 kJ mol⁻¹ with respect to the initial reactants. Such energy demands can be easily accomplished at high temperatures with

the entropy factor driving the reaction toward the cyclization followed by hydrogen atom loss, as supported by kinetic calculations (Supplementary Note 5). The corresponding values for the whole series of five cyclodehydrogenation reactions reveal narrow ranges in the intervals of 83–111 and 103–130 kJ mol⁻¹, respectively (Fig. 9 and Supplementary Fig. 10).

Overall, the results of kinetics and equilibrium calculations (Supplementary Figs. 8 and 9) reveal that the forward cyclodehydrogenation reactions, while being endoergic, strongly dominate at high temperatures; this finding allows us to conclude that once **p2** is synthesized in the gas phase, it can be efficiently converted into the C₄₀ nanobowl (C₄₀H₁₀, **p6**) through a series of five consecutive hydrogen abstraction – five-membered-cyclodehydrogenation stages under high-temperature conditions as in combustion flames. Alternatively, ultraviolet photons can also cleave the carbon-hydrogen bond in deep space. Interestingly, the hydrogen atoms or alternative abstracting radicals would play a dual role in this mechanism; on one hand, they promote the hydrogen abstraction reactions, which activate the otherwise stable PAH molecules but, on the other hand, the increase in their concentration shifts the equilibrium in unimolecular decomposition of the radical PAH species in the reverse direction. Overall, the C₄₀H₂₀ → C₄₀H₁₀ + 5H₂ reaction sequence catalyzed by hydrogen atoms can be classified as a subtype of hydrogen atom removal – cyclodehydrogenation reaction sequences.

Once a hydrogen atom is lost from the armchair edge of the C₄₀H₂₀–C₄₀H₁₂ molecules, the most favorable reaction pathway is the five-membered ring closure followed by a hydrogen loss as demonstrated above. The only alternative pathway is a hydrogen atom loss from the *ortho* position with respect to the radical to form an aromatic C-C triple bond forming an *o*-benzyne-like structure which is endoergic by about 335 kJ mol⁻¹; this energy is much higher than the energy needed for the cyclodehydrogenation reaction to occur. Clearly, the reaction scenario depends on which hydrogen atom is abstracted at the initial step of the reaction sequence. The hydrogen atom abstraction from an armchair edge unequivocally leads to cyclodehydrogenation (Supplementary

Fig. 10). Alternatively, hydrogen atom abstraction from outer carbon atoms of six-membered rings cannot be followed by cyclodehydrogenation directly. Here, possible scenarios would include bimolecular reactions of the radical with other species present, for example, yet another benzannulation via vinylacetylene addition, or acetylene addition – hydrogen atom elimination, or propargyl addition. This would result in a different growth pathway not leading to p6. The reaction can also proceed by hydrogen atom migration from the neighboring carbon atom at an armchair edge followed by cyclodehydrogenation. Such migrations have been demonstrated to be fast and highly probable at high temperatures by our recent kinetic Monte Carlo simulations of PAH growth⁴⁸. Also, in the presence of other radicals in the system, e.g., hydroxyl (OH), they can abstract hydrogen atoms from the $C_{40}H_x$ molecules with an even higher rate constant⁴⁷. Considering that the equilibrium constant for cyclodehydrogenation reactions grows with a decrease of the concentration of hydrogen atoms, the use of the radicals such as hydroxyl for the activating hydrogen atom abstraction step would further facilitate the reaction in the forward direction toward the formation of the nanobowl molecule.

A combination of a molecular beam experiment and isomer-selective detection of the reaction products with electronic structure and kinetics calculations allowed us to unravel the formation mechanism of benzocorannulene ($C_{24}H_{12}$) via ring annulation. Exploiting this prototype of benzannulation, we computationally elucidated viable pathways to the gas-phase synthesis of the C40 nanobowl ($C_{40}H_{10}$) via five consecutive benzannulation steps to pentabenzocorannulene ($C_{40}H_{20}$) followed by five five-membered ring closures at the armchair edges at high temperatures yielding the C40 nanobowl. The benzannulation steps can alternate with the hydrogen abstraction–cyclodehydrogenation steps; the latter becomes possible as soon as two neighboring outside six-membered rings of corannulene have been benzannulated. As a molecular building block of fullerene (C_{60}), we anticipate that such mechanisms could be common in the formation and growth of buckyballs and carbon nanotubes not only in combustion flames, but also in circumstellar

309 envelopes and planetary nebulae of carbon-rich stars, which feature similar temperatures. At any
310 particular environment, the mechanism is governed by the presence and abundance of hydrocarbon
311 species required for the addition steps (vinylacetylene, C_4H_4) and radicals (H, OH) driving the
312 hydrogen atom abstraction steps activating closed-shell PAH molecules partaking in the growth
313 process.

Methods

Experimental. The experiments were conducted at the X04DB beamline of the Swiss Light Source (SLS) at the Paul Scherrer Institute (PSI) utilizing a resistively heated silicon–carbide (SiC) chemical microreactor coupled to a molecular beam apparatus operated with a double velocity map imaging (VMI) photoelectron photoion coincidence spectrometer^{41,49-54}. This setup allows the exploration of molecular mass growth processes to aromatic molecules *in situ* via elementary reactions of pyrolytically generated aryl radicals. In detail, bromocorannulene (C₂₀H₉Br; synthesized in house) was sublimed at 443 ± 1 K in a high-vacuum oven in the source chamber and was seeded in vinylacetylene (C₄H₄; 5 % in helium, Applied Gas Inc.) at a backing pressure of 100 mbar. The gas mixture was introduced through a 200 μ m diameter nozzle into a 35 mm long SiC tube with 1 mm inner diameter at a heated length of 20 mm. Corannulenyl radicals (C₂₀H₉•) were created *in situ* via pyrolysis of bromocorannulene at a reactor temperature of 1200 ± 100 K measured by a type C thermocouple. These radicals react with the vinylacetylene reactant/seeding gas to form the products, which exit the microreactor and attain supersonic expansion before passing through a 2 mm diameter skimmer to the experimental chamber, which houses the photoelectron photoion coincidence (PEPICO) spectrometer. Here, the products were photoionized by quasi-continuous synchrotron vacuum ultraviolet (VUV) radiation tuned from 6.50 to 9.00 eV in 0.02 eV steps. VUV single-photon ionization represents a fragment-free technique and therefore is considered a soft ionization method^{55,56}. The ions and electrons formed via photoionization were extracted in opposing directions by a 218 V cm^{-1} electric field and were each imaged on separate position-sensitive delay-line anode detectors (Roentdek DLD40). The photoelectrons served as a time zero for the time-of-flight (TOF) measurement of the coincident photoion. Photoionization efficiency (PIE) curves, which report ion counts at a well-defined mass-to-charge ratio (m/z) as a function of photon energy, were obtained by integrating the signal at the specific m/z associated with the species of interest. Photoion mass-selective threshold

photoelectron (ms-TPE) spectra were obtained from the same scan by selecting only electrons with less than 10 meV kinetic energy, in coincidence with photoions in the mass range of interest. The hot electron signal, without an off-axis momentum, was subtracted from the threshold (low kinetic energy less than 10 meV) electron signal by the procedure of Sztaray et al⁵⁷. ms-TPES obtained from hot pyrolysis reactors often suffer from spectral broadening due to insufficient expansion cooling. However, by integrating solely the room temperature background velocity component in the ions' VMI, a reduction of hot band transitions can be achieved and gives rise to room temperature ms-TPES⁵⁸. All spectra were normalized to the photon flux and corrected by 11 meV due to the Stark shift at a constant electric field of 218 V cm⁻¹⁵⁹. PIE and ms-TPE calibration curves of benzocorannulene (C₂₄H₁₂; synthesized in house) were collected for comparison to the reactive experiments by subliming benzocorannulene at 473 ± 1 K in the high-vacuum oven and seeding it in helium (He; 99.996 %, PanGas) at a backing pressure of 130 mbar without pyrolysis.

Computational. The molecular parameters including geometries, rotational constants, and vibrational frequencies of the reactants, products, along with intermediates and transition states for the reactions of corannulenyl and tetrabenzocorannulenyl radicals with vinylacetylene proceeding on the [C₂₄H₁₃][•] and [C₄₀H₂₁][•] potential energy surfaces (PES), as well as for the hydrogen atom abstraction – cyclodehydrogenation reactions involving C₄₀H₂₀ and C₄₀H₁₂ were calculated using the density functional theory (DFT) B3LYP/6-311G(d,p) level of theory⁶⁰⁻⁶². Using the optimized geometries, single point energies were refined within more accurate wavefunction-based theoretical methods. For the smallest [C₂₀H₉][•] plus C₄H₄ system, we employed coupled cluster CCSD(T) and second-order Møller–Plesset perturbation theory MP2 calculations, with the final G3(MP2,CC) energy being computed as⁶³ $E[\text{G3(MP2,CC)}] = E[\text{CCSD(T)/6-31G(d)}] + E[\text{MP2/G3(Large)}] - E[\text{MP2/6-31G(d)}] + \text{ZPE}[\text{B3LYP/6-311G(d,p)}]$. The model chemistry G3(MP2,CC) approach provides chemical accuracy of 0.01–0.02 Å for bond lengths, 1–2° for

bond angles, and 3–6 kJ mol⁻¹ for relative energies of hydrocarbons, their radicals, reaction energies, and barrier heights in terms of average absolute deviations. In addition, the energies were recalculated using domain based local pair-natural orbital singles and doubles coupled cluster method perturbatively included connected triple excitations (DLPNO-CCSD(T))⁶⁴ with Dunning's cc-pVDZ and cc-pVQZ basis sets⁶⁵. This allowed us to compare the performance of DLPNO-CCSD(T) for PAH growth reactions with the well-established model chemistry method and also to evaluate the convergence of DLPNO-CCSD(T) results with respect to the basis set. Two methods, ONIOM2 {G3(MP2,CC):B3LYP/6-311G(d,p)}⁶⁵⁻⁶⁷ and DLPNO-CCSD(T)/cc-pVDZ, were used for the energy refinement of various structures on the C₄₀H₂₁ PES accessed by the tetracorannulenyl plus vinylacetylene reaction. The ONIOM2 approach has recently been shown to provide accurate energies for large PAH systems with a careful choice of model systems^{66,67}. Here, as compared to the real C₄₀H₂₁[•] radical, the model system excluded four extra benzo rings around the corannulene core in the tetracorannulenyl radical with the dangling valences of the outside carbon atoms being saturated by hydrogens. Thus, the stoichiometry of the model system was only [C₂₄H₁₃][•] making the G3(MP2,CC) calculations within the ONIOM2 scheme affordable. Finally, for hydrogen atom abstraction and cyclodehydrogenation reactions involving C₄₀H₂₀ and C₄₀H₁₂ we used the DLPNO-CCSD(T)/cc-pVDZ method judging from its performance for C₂₄H₁₃[•] and [C₄₀H₂₁][•]. The choice of an appropriate model system for ONIOM calculations here is challenging because the entire buckled carbon skeleton is involved in the cyclization reactions.

Adiabatic ionization energies of possible C₂₄H₁₂ products of the corannulenyl plus vinylacetylene reactions were computed using the G3(MP2,CC)//B3LYP/6-311G(d,p) method with zero point energy (ZPE) corrections; the expected accuracy in this case is ± 0.05 eV. Moreover, ionization Franck-Condon factors at 0 K needed for a comparison with the experimental ms-TPE spectra were calculated using B3LYP/cc-pVTZ-optimized geometries and corresponding vibrational frequencies of the neutral and cationic species using the methodology implemented by

Barone and co-workers⁶⁸. For benzocorannulene, Franck-Condon factors were additionally reevaluated at elevated temperatures utilizing the ezSpectra code by Krylov et al⁶⁹. Electronic excitation energies of the benzocorannulene cation were estimated within the time-dependent (TD)-DFT method⁷⁰ with the ω B97XD functional⁷¹ and cc-pVTZ basis set⁶⁴. All the ab initio and DFT calculations were carried out using the GAUSSIAN 16⁷² (B3LYP, ω B97XD, and evaluation of Franck-Condon factors at zero Kelvin), MOLPRO 2021⁷³ (CCSD(T) and MP2), and ORCA⁷⁴ (DLPNO-CCSD(T)) quantum chemistry program packages.

Finally, pressure- and temperature-dependent rate constants and product branching ratios for the corannulenyl/tetrabenzocorannulenyl plus vinylacetylene reactions and for cyclodehydrogenation of $[C_{40}H_{19}]^{\bullet}$ and $[C_{40}H_{11}]^{\bullet}$ produced by hydrogen atom abstractions from pentabenzocorannulene $C_{40}H_{20}$ and $C_{40}H_{11}$, respectively, were assessed using the Rice–Ramsperger–Kassel–Marcus Master equation (RRKM-ME) theoretical approach utilizing the MESS software package⁷⁵. Here, partition functions for local minima and transition states were computed within the Rigid-Rotor, Harmonic-Oscillator (RRHO) model. Tunneling corrections were included using asymmetric Eckart potentials. The Lennard-Jones parameters ε and σ were estimated based upon the molecular mass of the intermediates involved in each particular reaction as proposed by Wang and Frenklach⁷⁶ and the parameters for the nitrogen bath gas were taken from Vishnyakov et al⁷⁷. The exponential down model was employed to treat the collisional energy transfer in ME, with the temperature dependence of the range parameter α for the deactivating wing of the energy transfer function expressed as

$$\alpha(T) = \alpha_{300}(T/300 \text{ K})^n \quad (7)$$

where the values of $n = 0.85$ and $\alpha_{300} = 247 \text{ cm}^{-1}$ proposed as universal for hydrocarbons were adopted⁷⁸. Supplementary Data 1–4 include input files for the RRKM-ME calculations using MESS, which incorporate optimized Cartesian coordinates and computed vibrational frequencies for all structures considered in this work.

414

415 **Data Availability:** All data generated in this study are available in the main text and the
416 supplementary materials.

417

418 **References**

- 419 1 Kroto, H. W., Heath, J. R., O'Brien, S. C., Curl, R. F. & Smalley, R. E. C60:
420 Buckminsterfullerene. *Nature* **318**, 162-163, (1985).
- 421 2 Kroto, H. W., Fischer, J. E. & Cox, D. E. *The Fullerenes*. (Elsevier Science, 2012).
- 422 3 Bakry, R. *et al.* Medicinal applications of fullerenes. *Int. J. Nanomed.* **2**, 639, (2007).
- 423 4 Azizi-Lalabadi, M., Hashemi, H., Feng, J. & Jafari, S. M. Carbon nanomaterials against
424 pathogens; the antimicrobial activity of carbon nanotubes, graphene/graphene oxide,
425 fullerenes, and their nanocomposites. *Adv. Colloid Interface Sci.* **284**, 102250, (2020).
- 426 5 Wharton, T. & Wilson, L. J. Highly-iodinated fullerene as a contrast agent for X-ray
427 imaging. *Bioorg. Med. Chem.* **10**, 3545-3554, (2002).
- 428 6 Wu, Y.-T. *et al.* Multiethynyl corannulenes: synthesis, structure, and properties. *J. Am.*
429 *Chem. Soc.* **130**, 10729-10739, (2008).
- 430 7 Zoppi, L., Ferretti, A. & Baldrige, K. K. Static and field-oriented properties of bowl-
431 shaped polynuclear aromatic hydrocarbon fragments. *J. Chem. Theory Comput.* **9**, 4797-
432 4804, (2013).
- 433 8 Li, W., Zhou, X., Wang, Q., Xiong, Z. & Tian, W. Q. Structural, nonlinear optical, and
434 vibration properties of the C₄₀H₁₀ buckybowl modified with nitrogen atoms. *Int. J.*
435 *Quantum Chem.* **115**, 1553-1560, (2015).

- 436 9 Lee, J., Cho, S., Hwang, Y., Lee, C. & Kim, S. H. Enhancement of lubrication properties
437 of nano-oil by controlling the amount of fullerene nanoparticle additives. *Tribol. Lett.* **28**,
438 203-208, (2007).
- 439 10 Liu, D., Zhao, W., Liu, S., Cen, Q. & Xue, Q. Comparative tribological and corrosion
440 resistance properties of epoxy composite coatings reinforced with functionalized
441 fullerene C₆₀ and graphene. *Surf. Coat. Technol.* **286**, 354-364, (2016).
- 442 11 Scott, L. T. *et al.* Geodesic polyarenes with exposed concave surfaces. *Pure Appl. Chem.*
443 **71**, 209-219, (1999).
- 444 12 Zoppi, L., Martin-Samos, L. & Baldrige, K. K. Buckybowl superatom states: a unique
445 route for electron transport? *Phys. Chem. Chem. Phys.* **17**, 6114-6121, (2015).
- 446 13 Rabideau, P. W. & Sygula, A. in *Advances in theoretically interesting molecules* Vol. 3
447 (Ed.: Randolph P Thummel), 1-36 (JAI Press, Greenwich, CT, 1995).
- 448 14 Mehta, G., Shahk, S. R. & Ravikumarc, K. Towards the design of tricyclopenta [*def, jkl*,
449 *pqr*] triphenylene ('sumanene'): a 'bowl-shaped' hydrocarbon featuring a structural motif
450 present in C₆₀(buckminsterfullerene). *J. Chem. Soc., Chem. Commun.*, 1006-1008,
451 (1993).
- 452 15 Jemmis, E. D., Sastry, G. N. & Mehta, G. Synthetic strategies towards C₇₀: Molecular
453 mechanics and MNDO calculations on pinakene, C₂₈H₁₄ and related molecules. *J. Chem.*
454 *Soc., Perkin Trans. 2*, 437-441, (1994).
- 455 16 Priyakumar, U. D. & Sastry, G. N. First ab initio and density functional study on the
456 structure, bowl-to-bowl inversion barrier, and vibrational spectra of the elusive C_{3v}-
457 symmetric buckybowl: Sumanene, C₂₁H₁₂. *J. Phys. Chem. A* **105**, 4488-4494, (2001).
- 458 17 dos Santos, S. *et al.* C₆₀-derived nanobaskets: Stability, vibrational signatures, and
459 molecular trapping. *Nanotechnology* **20**, 395701, (2009).

- 460 18 Peng, L. & Scott, L. T. Interconversions of aryl radicals by 1, 4-shifts of hydrogen atoms.
461 A synthesis of benzo[*a*]corannulene. *J. Am. Chem. Soc.* **127**, 16518-16521, (2005).
- 462 19 Scott, L. T. *et al.* A short, rigid, structurally pure carbon nanotube by stepwise chemical
463 synthesis. *J. Am. Chem. Soc.* **134**, 107-110, (2012).
- 464 20 Dinadayalane, T. & Sastry, G. N. Synthetic strategies toward buckybowls and C₆₀:
465 Benzannulation is remarkably facile compared to cyclopentannulation. *Tetrahedron Lett.*
466 **42**, 6421-6423, (2001).
- 467 21 Dinadayalane, T. C., Priyakumar, U. D. & Sastry, G. N. Ring closure synthetic strategies
468 toward buckybowls: Benzannulation versus cyclopentannulation. *J. Chem. Soc., Perkin*
469 *Trans. 2*, 94-101, (2002).
- 470 22 Clayton, M. D. & Rabideau, P. W. Synthesis of a new C₃₂H₁₂ bowl-shaped aromatic
471 hydrocarbon. *Tetrahedron Lett.* **38**, 741-744, (1997).
- 472 23 Sastry, G. N., Jemmis, E. D., Mehta, G. & Shah, S. R. Synthetic strategies towards C₆₀.
473 Molecular mechanics and MNDO study on sumanene and related structures. *J. Chem.*
474 *Soc., Perkin Trans. 2*, 1867-1871, (1993).
- 475 24 Taylor, R., Langley, G. J., Kroto, H. W. & Walton, D. R. Formation of C₆₀ by pyrolysis
476 of naphthalene. *Nature* **366**, 728-731, (1993).
- 477 25 Becker, L., Poreda, R. J. & Bunch, T. E. Fullerenes: An extraterrestrial carbon carrier
478 phase for noble gases. *Proc. Natl. Acad. Sci. U. S. A.* **97**, 2979-2983, (2000).
- 479 26 Cami, J., Bernard-Salas, J., Peeters, E. & Malek, S. E. Detection of C₆₀ and C₇₀ in a
480 young planetary nebula. *Science* **329**, 1180-1182, (2010).
- 481 27 Dunk, P. W. *et al.* Closed network growth of fullerenes. *Nat. Commun.* **3**, 1-9, (2012).

- 482 28 Krätschmer, W., Lamb, L. D., Fostiropoulos, K. & Huffman, D. R. Solid C₆₀: a new form
483 of carbon. *Nature* **347**, 354-358, (1990).
- 484 29 Taylor, R., Hare, J. P., Abdul-Sada, A. a. K. & Kroto, H. W. Isolation, separation and
485 characterisation of the fullerenes C₆₀ and C₇₀: the third form of carbon. *J. Chem. Soc.,*
486 *Chem. Commun.*, 1423-1425, (1990).
- 487 30 Berné, O. & Tielens, A. G. Formation of buckminsterfullerene (C₆₀) in interstellar space.
488 *Proc. Natl. Acad. Sci. U. S. A.* **109**, 401-406, (2012).
- 489 31 Otero, G. *et al.* Fullerenes from aromatic precursors by surface-catalysed
490 cyclodehydrogenation. *Nature* **454**, 865-868, (2008).
- 491 32 Berné, O., Montillaud, J. & Joblin, C. Top-down formation of fullerenes in the interstellar
492 medium. *Astron. Astrophys.* **577**, A133, (2015).
- 493 33 Micelotta, E. R. *et al.* The formation of cosmic fullerenes from aromatic clusters.
494 *Astrophys. J.* **761**, 35, (2012).
- 495 34 Chuvilin, A., Kaiser, U., Bichoutskaia, E., Besley, N. A. & Khlobystov, A. N. Direct
496 transformation of graphene to fullerene. *Nat. Chem.* **2**, 450-453, (2010).
- 497 35 Bernal, J. *et al.* Formation of interstellar C₆₀ from silicon carbide circumstellar grains.
498 *Astrophys. J., Lett.* **883**, L43, (2019).
- 499 36 IUPAC name: 5,8,6,7-[1,3]Butadiene[1,3]diyl[4]ylidenebenz[5,6]-*as*-indaceno[7,8,1,2,3-
500 *defghi*]cyclopent[*kl*]-*as*-indaceno[3,2,1,8,7,6-*pqrstuv*]picene).
- 501 37 Traeger, J. C. A study of the allyl cation thermochemistry by photoionization mass
502 spectrometry. *Int. J. Mass Spectrom. Ion Process.* **58**, 259-271, (1984).

- 38 Mercier, X. *et al.* Selective identification of cyclopentaring-fused PAHs and side-substituted PAHs in a low pressure premixed sooting flame by photoelectron photoion coincidence spectroscopy. *Phys. Chem. Chem. Phys.* **22**, 15926-15944, (2020).
- 39 Bréchignac, P. *et al.* Photoionization of cold gas phase coronene and its clusters: Autoionization resonances in monomer, dimer, and trimer and electronic structure of monomer cation. *J. Chem. Phys.* **141**, 164325, (2014).
- 40 Bourgalais, J. *et al.* Jet-stirred reactor study of low-temperature neopentane oxidation: A combined theoretical, chromatographic, mass spectrometric, and PEPICO analysis. *Energy Fuels* **35**, 19689-19704, (2021).
- 41 Hemberger, P. *et al.* Photoelectron photoion coincidence spectroscopy provides mechanistic insights in fuel synthesis and conversion. *Energy Fuels* **35**, 16265-16302, (2021).
- 42 Hemberger, P. *et al.* A pass too far: dissociation of internal energy selected paracyclophane cations, theory and experiment. *Phys. Chem. Chem. Phys.* **14**, 11920-11929, (2012).
- 43 Pan, Z., Puente-Urbina, A., Bodi, A., van Bokhoven, J. A. & Hemberger, P. Isomer-dependent catalytic pyrolysis mechanism of the lignin model compounds catechol, resorcinol and hydroquinone. *Chem. Sci.* **12**, 3161-3169, (2021).
- 44 Rösch, D. *et al.* Absolute photoionization cross section of the simplest enol, vinyl alcohol. *J. Phys. Chem. A* **125**, 7920-7928, (2021).
- 45 Bodi, A., Hemberger, P., Osborn, D. L. & Sztáray, B. Mass-resolved isomer-selective chemical analysis with imaging photoelectron photoion coincidence spectroscopy. *J. Phys. Chem. Lett.* **4**, 2948-2952, (2013).

526 46 Kaiser, R. I. & Hansen, N. An aromatic universe – a physical chemistry perspective. *J.*
527 *Phys. Chem. A* **125**, 3826-3840, (2021).

528 47 Semenikhin, A. *et al.* Rate constants for H abstraction from benzo(a)pyrene and
529 chrysene: a theoretical study. *Phys. Chem. Chem. Phys.* **19**, 25401-25413, (2017).

530 48 Mebel, Alexander M. & Frenklach, M. Cleavage of an aromatic ring and radical
531 migration. *Faraday Discuss.* **238**, 512-528, (2022).

532 49 Bodi, A. *et al.* Imaging photoelectron photoion coincidence spectroscopy with velocity
533 focusing electron optics. *Rev. Sci. Instrum.* **80**, 034101, (2009).

534 50 Johnson, M., Bodi, A., Schulz, L. & Gerber, T. Vacuum ultraviolet beamline at the Swiss
535 Light Source for chemical dynamics studies. *Nucl. Instrum. Methods Phys. Res. A: Accel.*
536 *Spectrom. Detect. Assoc. Equip.* **610**, 597-603, (2009).

537 51 Bouwman, J., Bodi, A. & Hemberger, P. Nitrogen matters: the difference between PANH
538 and PAH formation. *Phys. Chem. Chem. Phys.* **20**, 29910-29917, (2018).

539 52 Hemberger, P., van Bokhoven, J. A., Pérez-Ramírez, J. & Bodi, A. New analytical tools
540 for advanced mechanistic studies in catalysis: photoionization and photoelectron
541 photoion coincidence spectroscopy. *Catal. Sci. Technol.* **10**, 1975-1990, (2020).

542 53 Mendez-Vega, E., Sander, W. & Hemberger, P. Isomer-selective threshold photoelectron
543 spectra of phenylnitrene and its thermal rearrangement products. *J. Phys. Chem. A* **124**,
544 3836-3843, (2020).

545 54 Grimm, S. *et al.* Gas-phase aluminium acetylacetonate decomposition: revision of the
546 current mechanism by VUV synchrotron radiation. *Phys. Chem. Chem. Phys.* **23**, 15059-
547 15075, (2021).

- 548 55 Qi, F. Combustion chemistry probed by synchrotron VUV photoionization mass
549 spectrometry. *Proc. Combust. Inst.* **34**, 33-63, (2013).
- 550 56 Cool, T. A. *et al.* Photoionization mass spectrometer for studies of flame chemistry with a
551 synchrotron light source. *Rev. Sci. Instrum.* **76**, 094102, (2005).
- 552 57 Sztáray, B. & Baer, T. Suppression of hot electrons in threshold photoelectron photoion
553 coincidence spectroscopy using velocity focusing optics. *Rev. Sci. Instrum.* **74**, 3763-
554 3768, (2003).
- 555 58 Hemberger, P., Wu, X., Pan, Z. & Bodi, A. Continuous pyrolysis microreactors: Hot
556 sources with little cooling? New insights utilizing cation velocity map imaging and
557 threshold photoelectron spectroscopy. *J. Phys. Chem. A* **126**, 2196-2210, (2022).
- 558 59 Chupka, W. A. Factors affecting lifetimes and resolution of Rydberg states observed in
559 zero-electron-kinetic-energy spectroscopy. *J. Chem. Phys.* **98**, 4520-4530, (1993).
- 560 60 Becke, A. D. Density-functional thermochemistry. III. The role of exact exchange. *J.*
561 *Chem. Phys.* **98**, 5648-5652, (1993).
- 562 61 Lee, C., Yang, W. & Parr, R. G. Development of the Colle-Salvetti correlation-energy
563 formula into a functional of the electron density. *Phys. Rev. B* **37**, 785-789, (1988).
- 564 62 Baboul, A. G., Curtiss, L. A., Redfern, P. C. & Raghavachari, K. Gaussian-3 theory using
565 density functional geometries and zero-point energies. *J. Chem. Phys.* **110**, 7650-7657,
566 (1999).
- 567 63 Riplinger, C., Sandhoefer, B., Hansen, A. & Neese, F. Natural triple excitations in local
568 coupled cluster calculations with pair natural orbitals. *J. Chem. Phys.* **139**, 134101,
569 (2013).

570 64 Dunning Jr., T. H. Gaussian basis sets for use in correlated molecular calculations. I. The
571 atoms boron through neon and hydrogen. *J. Chem. Phys.* **90**, 1007-1023, (1989).

572 65 Chung, L. W. *et al.* The ONIOM method and its applications. *Chem. Rev.* **115**, 5678-
573 5796, (2015).

574 66 Ao, C. *et al.* Toward high-level theoretical studies on the reaction kinetics of PAHs
575 growth based on HACA pathway: An ONIOM[G3(MP2,CC)//B3LYP:DFT] method
576 developed. *Fuel* **301**, 121052, (2021).

577 67 Savchenkova, A. S. *et al.* Mechanism of E-bridge formation by various PAH molecules:
578 A theoretical study. *Chem. Phys. Lett.* **799**, 139637, (2022).

579 68 Barone, V., Bloino, J., Biczysko, M. & Santoro, F. Fully integrated approach to compute
580 vibrationally resolved optical spectra: From small molecules to macrosystems. *J. Chem.*
581 *Theory Comput.* **5**, 540-554, (2009).

582 69 Gozem, S. & Krylov, A. I. The ezSpectra suite: An easy-to-use toolkit for spectroscopy
583 modeling. *WIREs Comput. Mol. Sci.* **12**, e1546, (2022).

584 70 Scalmani, G. *et al.* Geometries and properties of excited states in the gas phase and in
585 solution: Theory and application of a time-dependent density functional theory
586 polarizable continuum model. *J. Chem. Phys.* **124**, 094107, (2006).

587 71 Chai, J.-D. & Head-Gordon, M. Long-range corrected hybrid density functionals with
588 damped atom–atom dispersion corrections. *Phys. Chem. Chem. Phys.* **10**, 6615-6620,
589 (2008).

590 72 Frisch, M. J. *et al.* Gaussian 16 Rev. C.1 Gaussian, Inc., Wallingford, CT, (2019).

591 73 Werner, H. J. *et al.* MOLPRO, version 2021.2, a package of ab initio programs,
592 University of Cardiff: Cardiff, UK, see <http://www.molpro.net> (2021).

- 74 Neese, F. The ORCA program system. *WIREs Comput. Mol. Sci.* **2**, 73-78, (2012).
- 75 Georgievskii, Y. & Klippenstein, S. J. Master Equation System Solver [MESS], see
<https://tcg.cse.anl.gov/papr> (2015).
- 76 Wang, H. & Frenklach, M. Transport properties of polycyclic aromatic hydrocarbons for
flame modeling. *Combust. Flame* **96**, 163-170, (1994).
- 77 Neimark, A. V., Ravikovitch, P. I. & Vishnyakov, A. Adsorption hysteresis in nanopores.
Phys. Rev. E **62**, R1493-R1496, (2000).
- 78 Jasper, A. W., Oana, C. M. & Miller, J. A. “Third-Body” collision efficiencies for
combustion modeling: Hydrocarbons in atomic and diatomic baths. *Proc. Combust. Inst.*
35, 197-204, (2015).

Acknowledgments

This work was supported by the U.S. Department of Energy, Basic Energy Sciences, by Grant No. DE-FG02-03ER15411 to the University of Hawaii at Manoa and No. DE-FG02-04ER15570 to the Florida International University. We acknowledge the Instructional & Research Computing Center (IRCC, web: <http://ircc.fiu.edu>) at FIU and the National Energy Research Scientific Computing Center (NERSC) of the Office of Science in the U.S. Department of Energy for providing computing resources. The PEPICO measurements were performed at the VUV (x04db) beamline of the Swiss Light Source (SLS), located at Paul Scherrer Institute, Villigen Switzerland. We are thankful to Prof. Jay Siegel for his assistance with the synthesis of bromocorannulene.

Author Contributions

R.I.K. designed the experiment; S.J.G. and A.M.T. performed the experimental measurements; P.H. supervised the experiment; A.H.H. and T.G. synthesized the experimental precursor; S.F.W. supervised the precursor synthesis; S.J.G. performed the data analysis; L.B.T. carried out the

618 theoretical analysis; A.M.M. supervised the theoretical analysis; L.B.T., S.J.G., P.H., A.M.M.,
619 and R.I.K. wrote the paper.

620

621 **Competing interests**

622 The authors declare no competing interests.

Figures

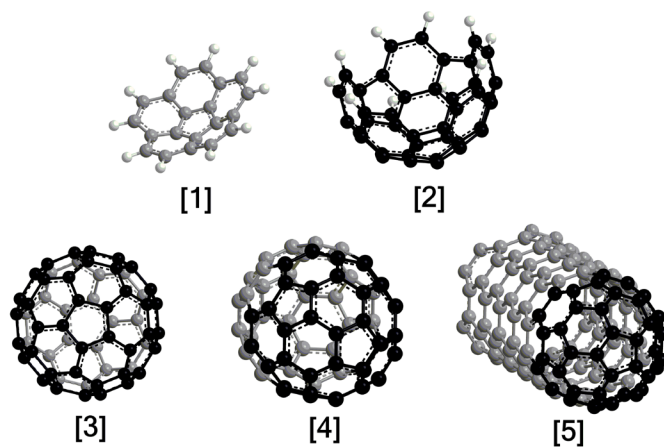
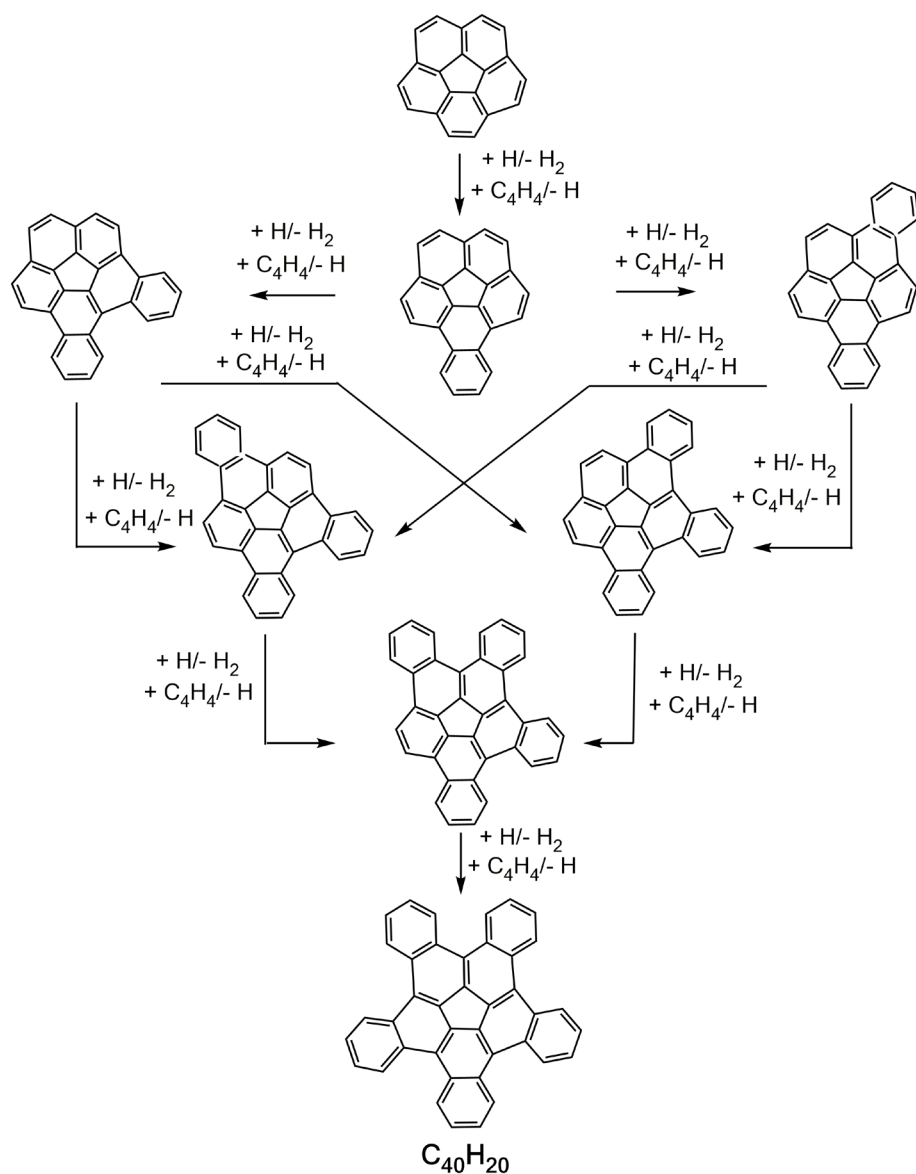


Fig. 1 Molecular structures of 3-dimensional carbonaceous nanostructures. The smallest nanobowl, corannulene [1], as well as the C40 nanobowl [2] emphasized as a molecular building block of Buckminsterfullerene (C_{60}) [3], rugbyballene (C_{70}) [4], and end-capped (5,5) armchair nanotubes [5]. The C40 nanobowl carbons are black, the remaining carbons are grey, and hydrogen is white.



632

633 **Fig. 2 Pathways for the corannuleny-vinylacetylene reaction.** Schematic representation of

634 reaction pathways to pentabenzocorannulene (C₄₀H₂₀).

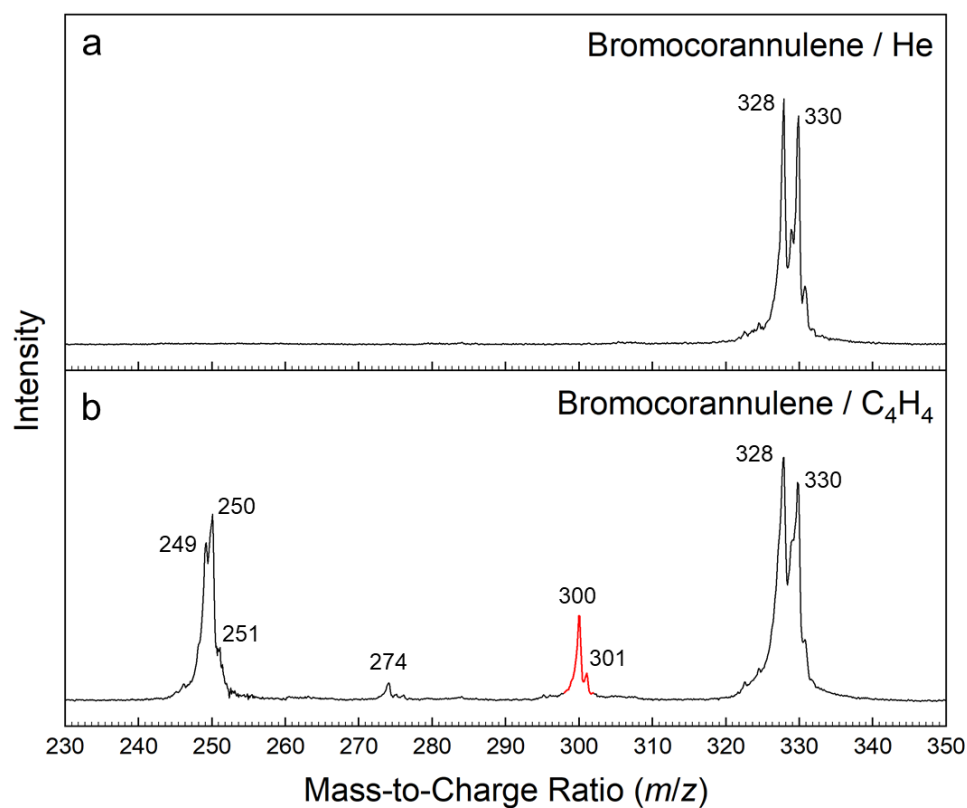


Fig. 3 Photoionization mass spectra. Comparison of mass spectra taken at a photon energy of 9.00 eV. **(a)** bromocorannulene (C₂₀H₉Br) – helium (He) system; **(b)** bromocorannulene (C₂₀H₉Br) – vinylacetylene (C₄H₄) system at a reactor temperature of 1200 ± 100 K. The mass peaks of the newly formed C₂₄H₁₂ (m/z = 300) species along with the ¹³C-substituted counterparts (m/z = 301) are highlighted in red.

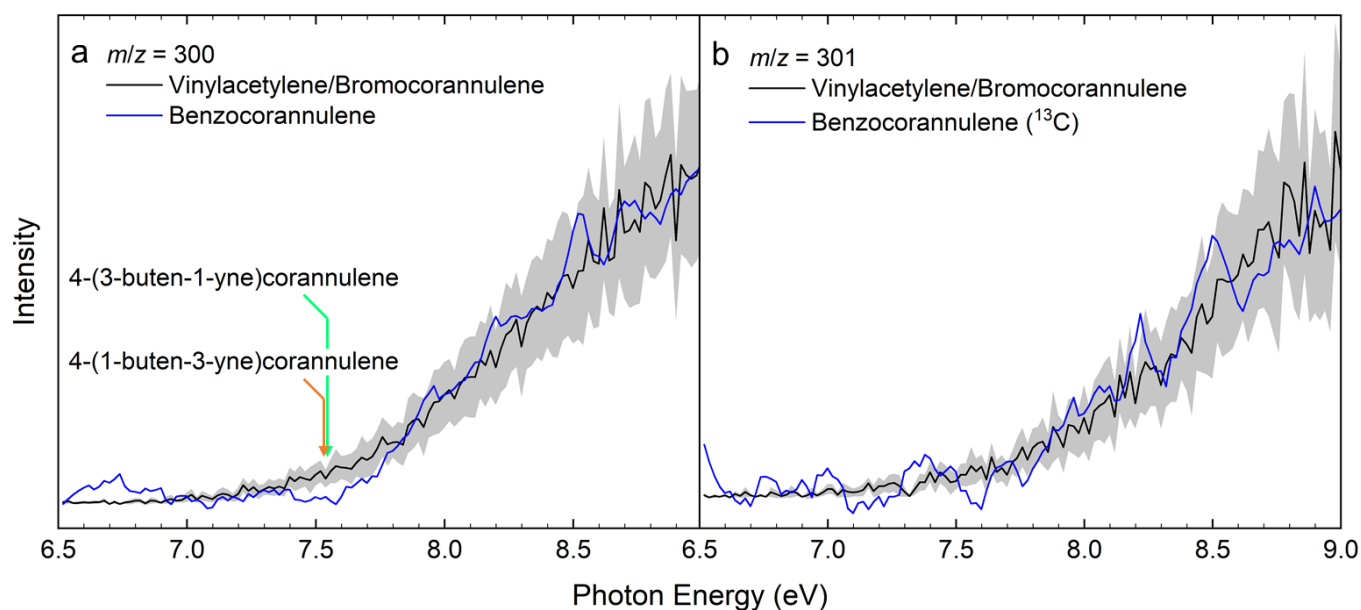


Fig. 4 Photoionization efficiency (PIE) curves. PIE curves relevant to the formation of benzocorannulene. (a) $m/z = 300$ ($C_{24}H_{12}$) and (b) $m/z = 301$ ($^{13}CC_{23}H_{12}$). Black: experimentally derived PIE curve; blue: benzocorannulene PIE curve; green: calculated ionization onset of *trans*-4-(1-buten-3-yne)corannulene; orange: calculated ionization onset of *cis*-4-(3-buten-1-yne)corannulene. The overall error bars (gray area) consist of two parts: 1 σ error of the PIE curve averaged over the individual scans and $\pm 10\%$ based on the accuracy of the photodiode.

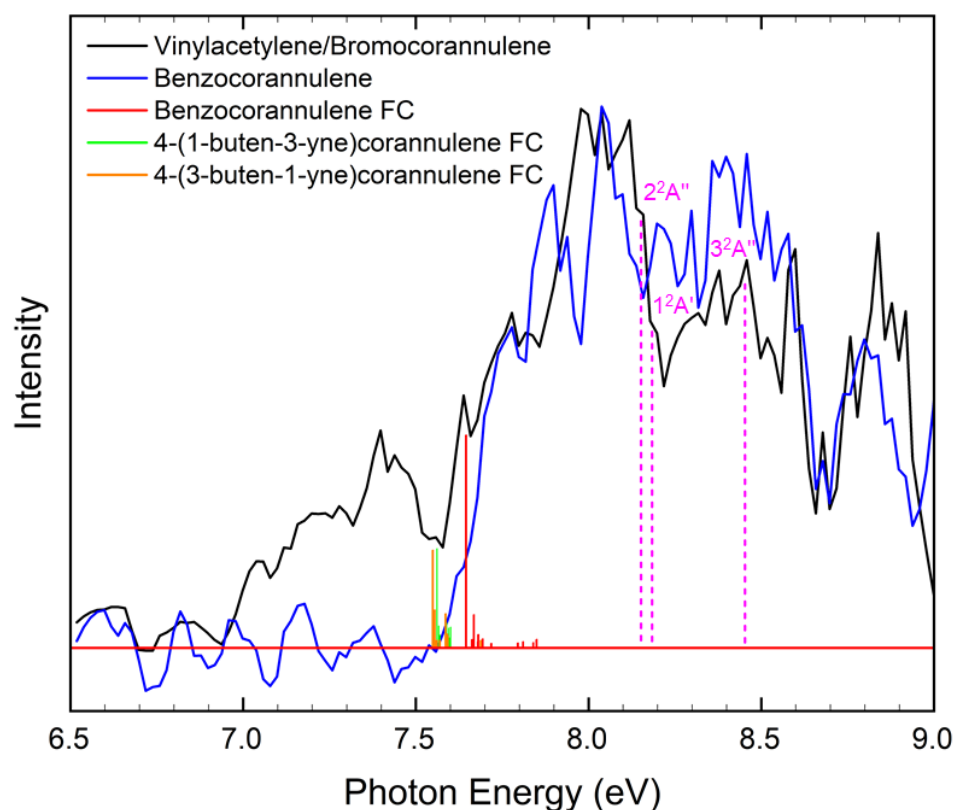


Fig. 5 Mass-selected threshold photoelectron (ms-TPE) spectra. Photoion ms-TPE spectra relevant to the formation of benzocorannulene at $m/z = 300$ ($C_{24}H_{12}$). Black: experimentally derived ms-TPE spectrum; blue: benzocorannulene ms-TPE spectrum; red: Franck-Condon (FC) stick spectrum for benzocorannulene; green: FC spectrum for *trans*-4-(1-buten-3-yne)corannulene; orange: FC spectrum for *cis*-4-(3-buten-1-yne)corannulene; magenta: calculated ionization energies of 8.152, 8.184, and 8.453 eV corresponding to the $2^2A''$, $1^2A'$, and $3^2A''$ electronic excited states of the benzocorannulene cation.

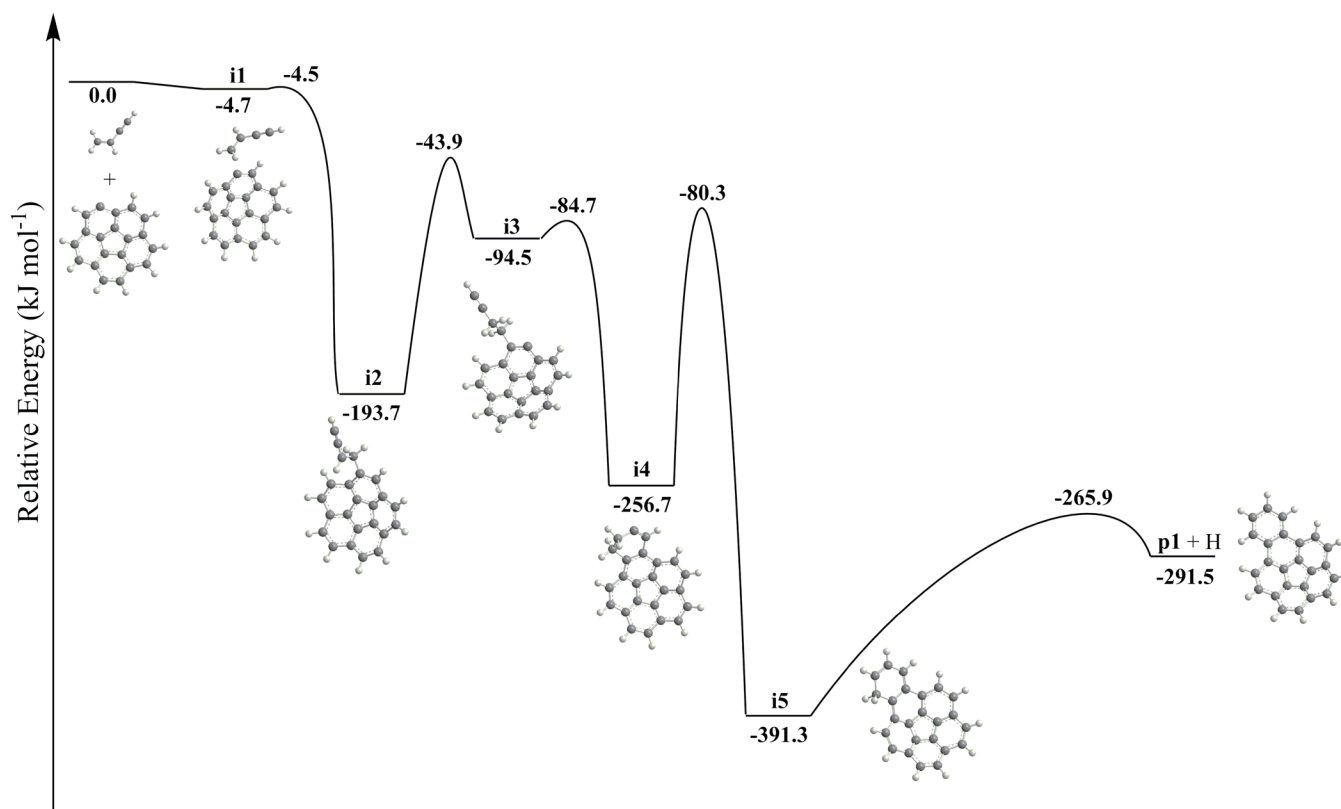


Fig. 6 Potential energy diagram leading to benzocorannulene. Calculated potential energy diagram for the $[C_{20}H_9]^+$ plus vinylacetylene reaction. Relative energies of various species calculated at the DLPNO-CCSD(T)/cc-pVDZ level of theory are given in kJ mol⁻¹ with respect to the initial reactants. A full version of the diagram and the Cartesian coordinates are available in Supplementary Fig. 6 and Supplementary Data 1. Energies are calculated with chemical accuracy of about 10 kJ mol⁻¹. Carbon atoms are grey and hydrogen atoms are white.

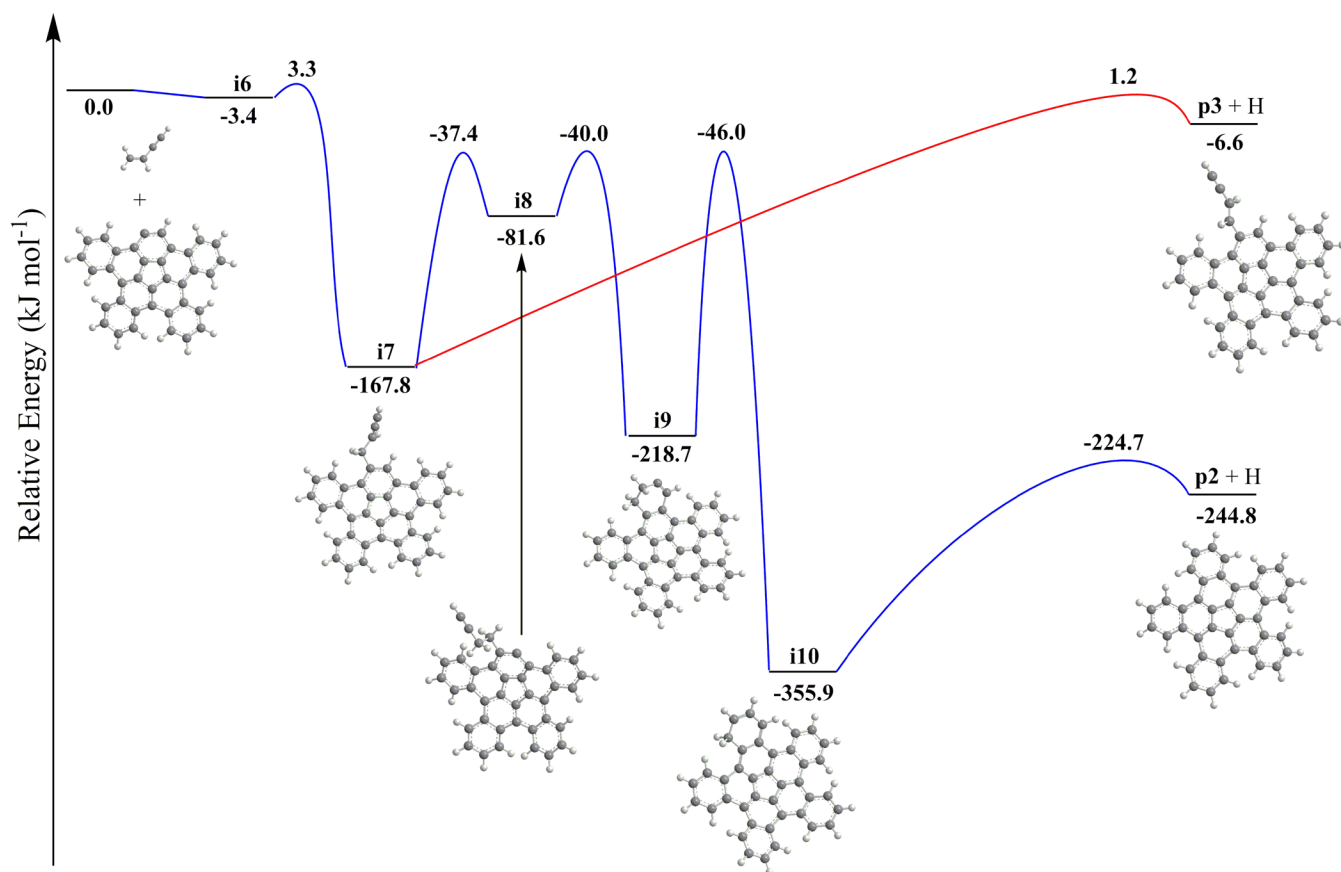
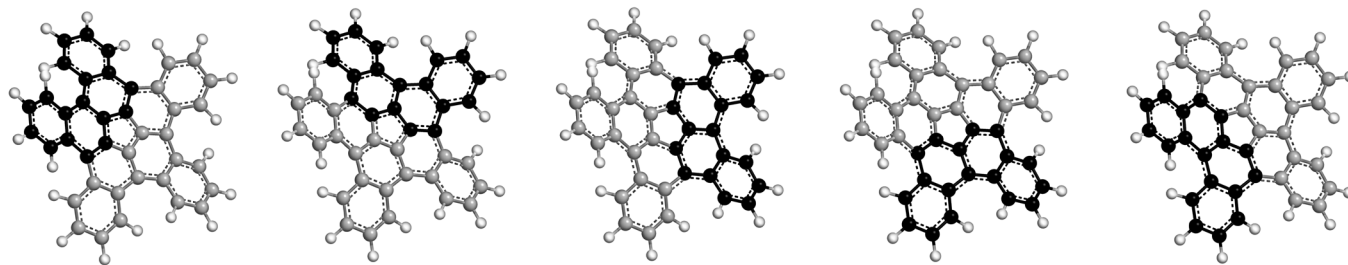


Fig. 7 Potential energy diagram leading to pentabenzocorannulene. Calculated potential energy diagram for the most important channels of the $[C_{36}H_{17}]^+$ plus vinylacetylene reaction. Relative energies of various species calculated at the DLPNO-CCSD(T)/cc-pVDZ level of theory are given in kJ mol⁻¹ with respect to the initial reactants. A full version of the diagram and Cartesian coordinates are available in Supplementary Fig. 7 and Supplementary Data 2. Carbon atoms are grey and hydrogen atoms are white.



670

671 **Fig. 8 [4]-Helicene units in pentabenzocorannulene.** Five overlapping [4]-helicene moieties in

672 the structure of pentabenzocorannulene. Carbon atoms in each [4]-helicene unit are highlighted

673 in black, the remaining carbon atoms are grey, and hydrogen atoms are white.

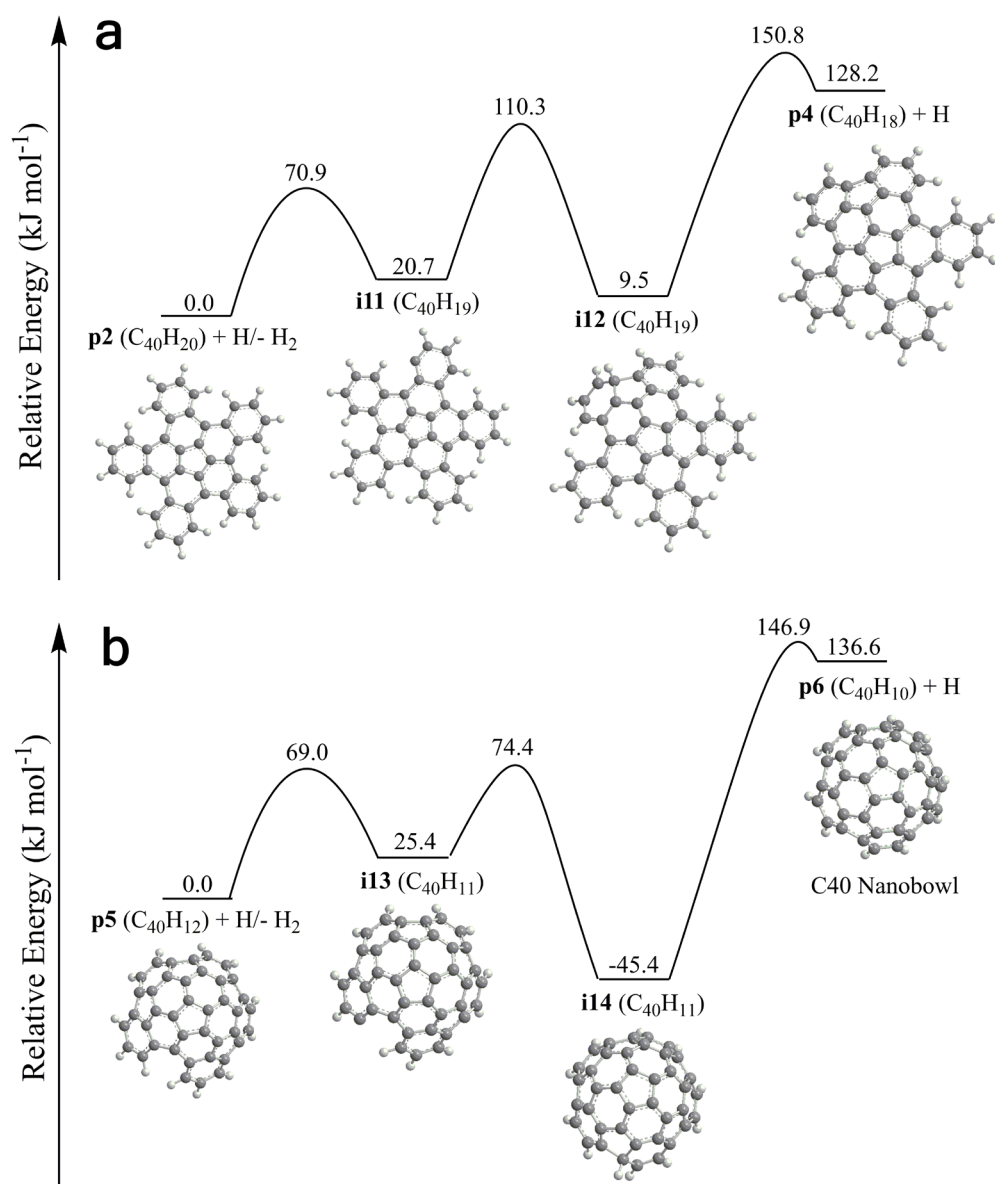


Fig. 9 Potential energy diagram leading to the C40 nanobowl. Calculated potential energy diagrams for the conversion of pentabenzocorannulene ($\text{C}_{40}\text{H}_{20}$) to $\text{C}_{40}\text{H}_{18}$ (**a**) and $\text{C}_{40}\text{H}_{12}$ to the C40 nanobowl ($\text{C}_{40}\text{H}_{10}$) (**b**) via a hydrogen abstraction – cyclodehydrogenation mechanism. Relative energies of various species calculated at the DLPNO-CCSD(T)/cc-pVDZ level of theory are given in kJ mol^{-1} with respect to the initial reactants. A full version of the diagram for all five hydrogen atom abstraction – cyclodehydrogenation steps along with the Cartesian coordinates is available in Supplementary Fig. 10 and Supplementary Data 3 and 4. Carbon atoms are grey and hydrogen atoms are white.

Supplementary Information

Gas Phase Synthesis of the C₄₀ Nano Bowl C₄₀H₁₀

Tuli et al.

Supplementary Note 1: Theoretical methods performance comparison in potential energy diagram calculations.

For the corannulenyl reaction considered here, there is a close agreement between the relative energies computed by our standard G3(MP2,CC) level and those obtained at DLPNO-CCSD(T) both with the cc-pVDZ and cc-pVQZ basis sets (see Supplementary Fig. 6 and Supplementary Table 1). The differences are normally within 3 kJ mol⁻¹ for the ring annulation pathway but somewhat larger, up to 11 kJ mol⁻¹, for the 4-(1-buten-3-yne)corannulene and 4-(3-buten-1-yne)corannulene products and the respective hydrogen atom loss transition states. Also, the DLPNO-CCSD(T) results with the cc-pVDZ and cc-pVQZ basis sets are very close to one another with few exceptions (**i4** and **p1**), where the deviation is 8-9 kJ mol⁻¹. This comparison indicates that the chemical accuracy of about 10 kJ mol⁻¹ can be normally achieved for molecules of this type employing the DLPNO-CCSD(T)/cc-pVDZ level of theory opening the opportunity to carry out accurate calculations for much larger systems than those treatable by the model chemistry G3/G4-type schemes. One can also see that the accuracy of DFT relative energies is not sufficient, with discrepancies from the more accurate results often exceeding 40 kJ mol⁻¹ and not being consistent.

The calculations of the [C₃₆H₁₇][•] + C₄H₄ potential energy diagram were additionally carried out at the ONIOM2(G3(MP2,CC):B3LYP/6-311G(d,p)) level of theory, where the central corannulene moiety was chosen as the model system, with four outside six-membered rings removed and replaced by H atoms saturating the dangling bonds. The agreement between the DLPNO-CCSD(T)/cc-pVDZ and ONIOM relative energies is reasonably close, with the average absolute deviation of 5.8 kJ mol⁻¹ (Supplementary Fig. 7 and Supplementary Table 1). The largest discrepancy of 12.6 kJ mol⁻¹ is found for **i9** where the ONIOM value underestimates the DLPNO-CCSD(T) calculated well depth. Nevertheless, it is evident that both DLPNO-CCSD(T)/cc-pVDZ and ONIOM methods represent viable alternative for calculations of large PAH systems with nearly chemical accuracy. Again, the deviations of B3LYP energies from the more accurate results are significantly higher.

Supplementary Note 2: Alternative pathways in the $[\text{C}_{20}\text{H}_9]^{\bullet} + \text{C}_4\text{H}_4$ reaction.

In a competing reaction pathway, **i2** can directly dissociate to *trans*-4-(3-buten-1-yne)corannulene **p9** by splitting a hydrogen atom from the α carbon in the side chain (Supplementary Fig. 6). The transition state for the hydrogen atom loss and the **p9** + H products reside at 22 and 41 kJ mol^{-1} lower in energy than the reactants (in this Section we discuss the values obtained at the G3(MP2,CC) level of theory which was routinely used for all structures). Also, **i2** can rearrange to **i16** by shifting the corannulene moiety over the $\text{CH}_2\text{-CH}$ bond in the side chain overcoming a 104 kJ mol^{-1} barrier. Intermediate **i16** can be formed from the initial complex **i1** by linking the radical site in $[\text{C}_{20}\text{H}_9]^{\bullet}$ with the C2 atom of vinylacetylene via a transition state positioned 5 kJ mol^{-1} above the reactants. Next, **i16** can lose the hydrogen atom from the attacked C2 carbon forming the **p8** product 3-(3-buten-1-yne)corannulene exoergic by 36 kJ mol^{-1} via a transition state lying 3 kJ mol^{-1} above the reactants. In an alternative pathway, **i16** can feature a shift of the terminal side chain CH group over the CH-CH_2 bond producing a three-membered ring in **i17**, with the following ring opening rendering the **i18** intermediate with a CHCH_2CCH side chain attached to the corannulenyl radical. Note that **i18** can be also achieved directly from **i2** by a 1,2-H shift in the side chain but via a significantly higher barrier of 188 kJ mol^{-1} relative to **i2**. The **i16** \rightarrow **i17** \rightarrow **i18** isomerization is expected to be fast as it involves rather low ring closure/opening barriers. Subsequently, **i18** can dissociate to both *trans*- and *cis*-conformers of 4-(3-buten-1-yne)corannulene via transition states located 17 and 18 kJ mol^{-1} below the separated reactants ($[\text{C}_{20}\text{H}_9]^{\bullet}/\text{C}_4\text{H}_4$), respectively. The *cis*-4-(3-buten-1-yne)corannulene conformer is 7 kJ mol^{-1} higher in energy than the *trans*-conformer. Vinylacetylene can also add to the corannulenyl radical by its acetylenic C4 atom producing the intermediate **i15**. The pathway to the latter from the van der Waals complex **i1** proceeds through a low barrier of $\sim 7 \text{ kJ mol}^{-1}$, which is submerged by 0.4 kJ mol^{-1} relative to the reactants. In turn, **i15** can dissociate by losing the hydrogen atom from C4 forming 4-(1-buten-3-yne)corannulene **p7** residing 49 kJ mol^{-1} below the reactants via a transition state at 28 kJ mol^{-1} lower in energy than the reactants.

Besides the vinylacetylene addition pathways described above and in the main text, the $[\text{C}_{20}\text{H}_9]^{\bullet} + \text{C}_4\text{H}_4$ reaction can proceed by direct hydrogen atom abstraction from vinylacetylene by the corannulenyl radical forming *i*- and *n*- C_4H_3 plus $\text{C}_{20}\text{H}_{10}$ (corannulene) via respective barriers of 16 and 32 kJ mol^{-1} . The abstraction reactions are calculated to be 51 kJ mol^{-1} exoergic for *i*-

C_4H_3 and 1 kJ mol^{-1} endoergic for $n\text{-}C_4H_3$. Note that other reaction pathways (e.g., vinylacetylene addition by C3 carbon atom or a lengthy isomerization pathway leading from **i15** to the **p1** + H products) are also possible as described in great detail for the prototype phenyl plus vinylacetylene reaction¹, but in this present study, we focus only on the channels which were proved to be most significant in this reaction class and lead to the experimentally observed products of the $[C_{20}H_9]^+$ plus C_4H_4 reaction.

Supplementary Note 3: Comparison of vinylacetylene addition reactions to various PAH radicals.

It is informative to compare the corannulenyl plus vinylacetylene potential energy diagram computed here with those for the reactions of other PAH radicals with C_4H_4 ²⁻⁴ focusing on the most relevant, for PAH growth, ring annulation channel and the competitive H loss pathways (Table S1). There is a large similarity of the relative energies computed here and in the previous works, especially with the 2-tetracenyl + C_4H_4 reaction channels leading to benzo[a]tetracene and its **p9**- and **p7**-like isomers³. The differences for most species do not exceed 5 kJ mol⁻¹ and the largest one, 23 kJ mol⁻¹, is observed for the six-membered ring closure transition state **i3-i4**. As compared to the smaller reacting radicals, phenyl and 1-naphthyl, corannulenyl has small but consistent stabilization of all intermediates, transitions states, and the benzannulated product along the ring annulation pathway. Also peculiar is that the barrier for vinylacetylene addition by the acetylenic C4 atom is clearly reduced for corannulenyl as compared to the other PAH radicals previously studied and even becomes slightly submerged at the G3(MP2,CC) level, while remaining marginally positive at DLPNO-CCSD(T). Generally, Table S1 demonstrates that the ring annulation reactions involving PAH radicals proceed by similar mechanisms although their quantitative details may somewhat vary depending on the size and shape of the reacting radical and the final expanded PAH product.

Supplementary Note 4: Kinetics of the $[\text{C}_{20}\text{H}_9]^{\bullet}$ plus C_4H_4 Reaction.

The multichannel kinetics of benzannulation of aryl radicals with vinylacetylene is rather complex as multiple products can be formed, with their relative yields strongly depending on temperature and pressure. The formation of the most thermodynamically favorable benzannulated product, benzocorannulene, is strongly preferred at low temperatures and very low pressures which would exclude collisional stabilization of intermediate potential wells. As the pressure increases, the dominating low-temperature products, up to at least 1,000 K, are stabilized $[\text{C}_{24}\text{H}_{13}]^{\bullet}$ intermediates including **i15**, **i2**, **i4**, and **i18**. At high temperatures relevant to the present experiment as well as to the conditions in combustion flames and circumstellar envelopes, the formation of the side-chained $\text{C}_{24}\text{H}_{12}$ isomers, such as **p7**, **p9**, and **p10**, is preferred (Supplementary Fig. 8(a)). The rate constant to produce **p1** at 1,200 K and 0.03 atm, which represents typical conditions inside the microreactor, is reasonably high, $3.4 \times 10^{-14} \text{ cm}^3 \text{ molecule}^{-1}$, but the relative yield of **p1** in the primary reaction is predicted to be low as compared to **p7**, **p9**, and **p10**. However, the **p7**, **p9**, and **p10** isomers of $\text{C}_{24}\text{H}_{12}$, in addition to their mutual hydrogen-assisted isomerization and the reversal back to the initial reactants, can also efficiently convert to the much more stable **p1** species in the secondary reactions with H atoms (Supplementary Fig. 8(b)). For instance, the calculated rate constants for the **p10/p9** + H \rightarrow **p1** + H reactions are on the order of $3 \times 10^{-13} \text{ cm}^3 \text{ molecule}^{-1}$ under the reactor conditions. Although not particularly explored here due to the complexity of the channels involved, based on the analogy with phenyl plus vinylacetylene, the secondary **p7** + H reaction is anticipated to mostly produce the reactants as well as **p9** + H and **p1** + H. Our simulations of the chemical and physical processes inside the microreactor for phenyl plus vinylacetylene¹ have demonstrated that the analogs of **p9** and **p7** predominantly form first in the primary reaction and then are eventually converted to **p1** through secondary H-assisted reactions. A similar behavior might explain the formation of benzocorannulene as the prevailing product exiting the microreactor and identified in the present experiment at elevated temperatures. However, at conditions resembling cold molecular clouds (10 K), **p1** can be primarily formed via reaction of corannulenyl plus vinylacetylene.

Supplementary Note 5: Kinetics of cyclodehydrogenation reactions.

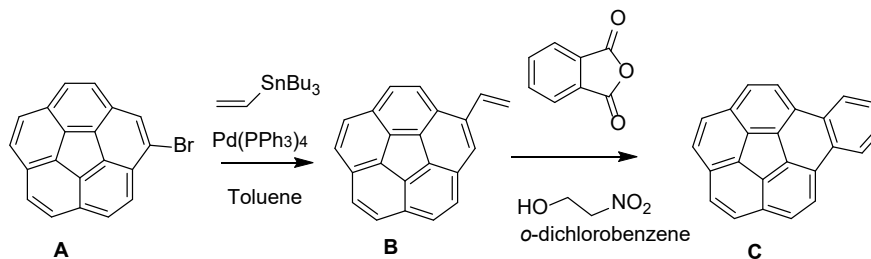
The kinetics of hydrogen abstraction from PAH molecules is well known⁵ and this process is firmly established to play an important role in the growth of carbonaceous species and nanostructures⁶. Therefore, here we focus on unimolecular decomposition of the $[C_{40}H_{19}]^*$ and $[C_{40}H_{11}]^*$ radicals via cyclodehydrogenation to demonstrate that this process is indeed favorable at high temperatures. Supplementary Fig. 9 shows calculated reaction rate constants in the forward and reverse directions and equilibrium constants. The decomposition of $[C_{40}H_{19}]^*$ **i11** occurring through the five-membered ring closure followed by hydrogen loss is fast, with the rate constant at 1 atm reaching the values of 2.0×10^5 and $3.0 \times 10^7 \text{ s}^{-1}$ at 1000 and 1500 K, respectively. **i11** survives as a distinct chemical species up to 1125, 1500, and 1800 K at the pressures of 0.03, 1, and 10 atm, respectively, and fully equilibrates (merges) with its decomposition product $C_{40}H_{18}$ **p4** at higher temperatures. A slightly different kinetic behavior is predicted for $[C_{40}H_{11}]^*$. Here, the **i13** intermediate is significantly less stable than **i14** being separated from the latter by a rather low barrier. The rate constant for the **i13** \rightarrow **i14** isomerization is very fast even at 500 K ($1.7 \times 10^7 \text{ s}^{-1}$) and hence **i13** merges with **i14** at or above the temperatures of 500, 600, and 800 K at 0.03, 1, and 10 atm. Therefore, we considered rate constants for unimolecular decomposition of **i14** (Supplementary Fig. 9(b)). Those are also high, amounting to 1.2×10^4 and $1.9 \times 10^7 \text{ s}^{-1}$ at 1000 and 1500 K, respectively, at the atmospheric pressure. **i14** equilibrates with $C_{40}H_{10}$ **p6** + H at temperatures above 1250, 1500, 1750, and 2000 K at the pressures of 0.03, 1, 10, and 100 atm, respectively. Thus, $[C_{40}H_{11}]^*$ is more stable than $[C_{40}H_{19}]^*$, but its lifetime with the respect to the hydrogen atom loss is expected to be on a sub-microsecond scale at 1500 K and higher temperatures. On the other hand, the reverse bimolecular rate constants for $C_{40}H_{18} + H$ and $C_{40}H_{10} + H$ are also fast (Supplementary Fig. 9(c)), in the range of $2\text{-}3 \times 10^{-12} \text{ cm}^3 \text{ molecule}^{-1} \text{ s}^{-1}$ in the 1000-1500 K temperature interval at 1 atm for the former and $1\text{-}2 \times 10^{-10} \text{ cm}^3 \text{ molecule}^{-1} \text{ s}^{-1}$ for the latter. Those values are significantly higher than a competitive per site hydrogen abstraction⁵ from an armchair PAH edge. All this is indicative of rapid equilibration between the radicals and hydrogen loss products if the hydrogen atoms remain available for the reverse reaction and are not consumed by other processes. It is therefore informative to consider the equilibrium constants, which depend on the mole fraction x_H of available hydrogen atoms (Supplementary Fig. 9(d)). In order to test this hypothesis, we computed K_{eq} at two hydrogen mole fraction values typical in

combustion flames, 0.0004 and 0.01⁷. We found that the **i11** \rightleftharpoons C₄₀H₁₈ + H and **i13** \rightleftharpoons C₄₀H₁₈ + H equilibria rapidly shift in the forward direction with increasing temperature exceeding unity at 800 and 1000 K for [C₄₀H₁₉][•] and at 900 and 1125 K for [C₄₀H₁₁][•] respectively at the x_H values of 0.0004 and 0.01. At a typical combustion temperature of 1500 K, the values of K_{eq} rise to 4.3×10³ and 1.7×10² for [C₄₀H₁₉][•] and to 2.1×10³ and 8.3×10¹ for [C₄₀H₁₁][•] and the forward reactions dominate even stronger at higher temperature.

Supplementary Methods

Synthesis of bromocorannulene. Synthesis of bromocorannulene was carried out using the procedure given by Xu et al⁸. Briefly, to a 50 mL round-bottom flask, corannulene (1.0 g, 4.0 mmol) and *N*-bromosuccinimide (NBS) (712.0 mg, 4.0 mmol) were dissolved in 20 mL dichloroethane, then $\text{BF}_3 \cdot \text{Et}_2\text{O}$ (0.2 mL, 1.6 mmol) was added. The mixture was stirred at r.t. for 12 h and then quenched by 50 mL 10 % NaOH solution and extracted by DCM (2×50 mL). The organic layer was gathered and washed with water (2×50 mL) and dried using anhydrous Na_2SO_4 . The solvent was evaporated under vacuum and a crude product (total weight: 1.21 g) was obtained. The conversion rate (79.1%) and yield of bromocorannulene (69.3 %, 87.5 % b.r.s.m.) was determined by analytical HPLC. The crude reaction mixture of corannulene, bromocorannulene, and dibromocorannulene was packed on a short silica plug and separated into two portions (portion a: total weight 515 mg, 90 % bromocorannulene/ 10 % dibromocorannulene; portion b: total weight 685 mg, 30 % corannulene/ 65 % bromocorannulene/ 5 % dibromocorannulene). Portions a and b were then dissolved in HPLC grade DCM and mixed with kieselguhr, respectively, before undergoing further separation using Combiflash-Rf. The separation process obtained 955 mg 98 % pure bromocorannulene in total, as well as recovered 200 mg 98 % pure corannulene. $^1\text{H-NMR}$ data of bromocorannulene is consistent with reported values.

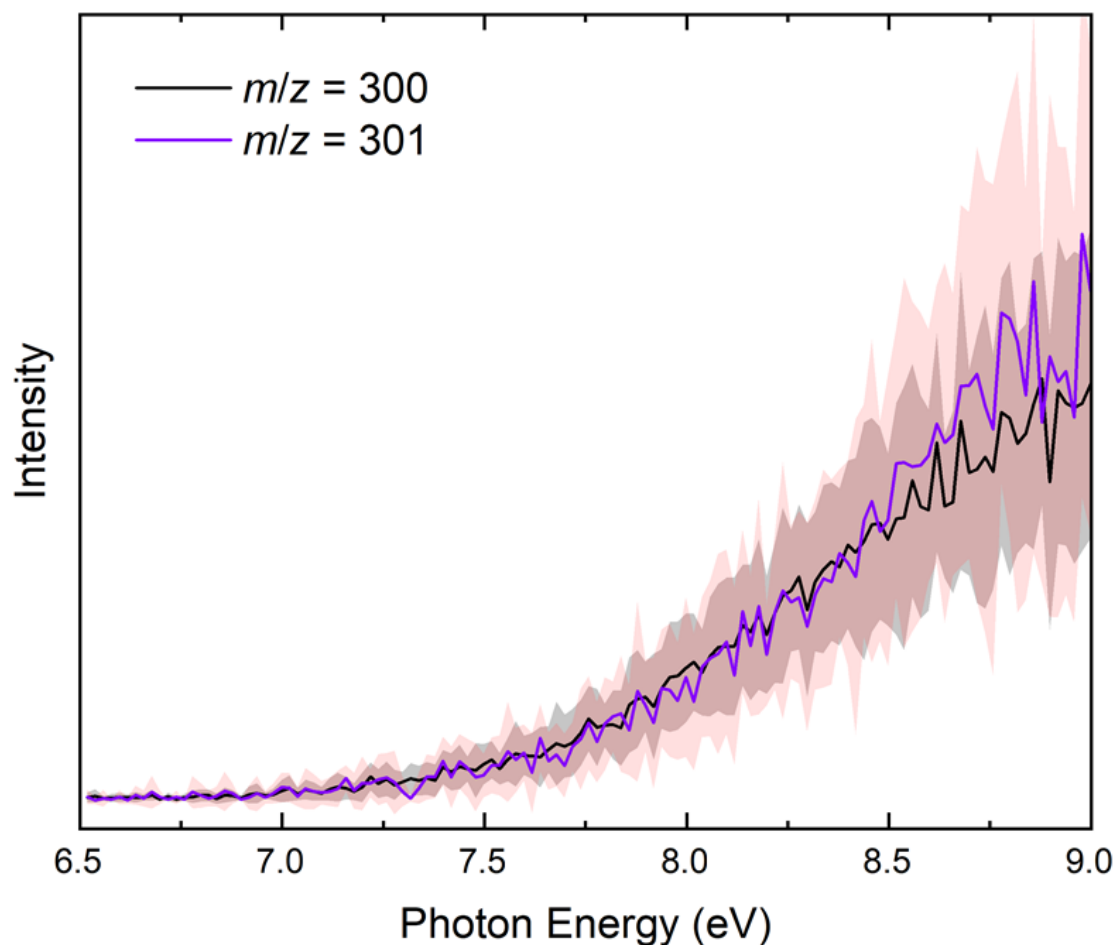
Synthesis of benzocorannulene C. Benzocorannulene has been synthesized from bromocorannulene A, which in turn has been prepared from corannulene by reported bromination protocol^{9,10}. The Pd-catalyzed Stille cross-coupling reaction of A with $\text{Bu}_3\text{Sn}(\text{vinyl})$ in toluene at 100 °C for 3 h afforded vinylcorannulene B³ (52%; Supplementary Fig. 1). Subsequent reaction of B with nitroethanol in the presence of phthalic anhydride in *o*-dichlorobenzene at 180 °C for 3 days provided C³ (28%).



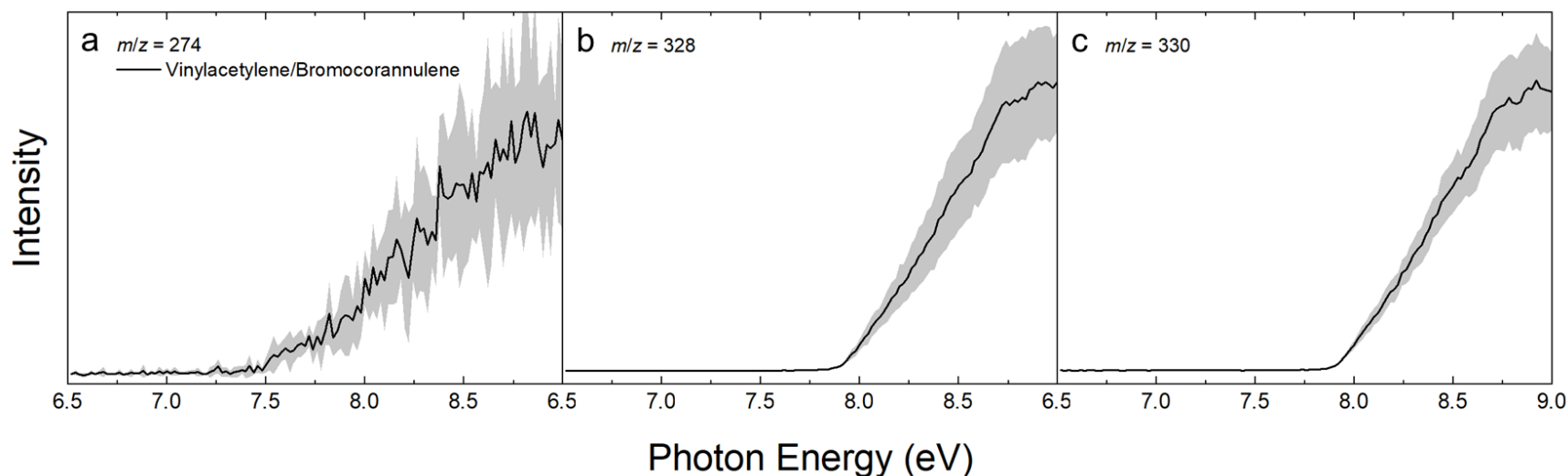
Supplementary Fig. 1. Synthesis of C

1-Vinylcorannulene (B). The **A**¹ (198 mg, 0.6 mmol) was dissolved in dry toluene (10 mL) in a flame-dried flask. Then Pd(PPh₃)₄ (23.2 mg, 0.02 mmol) and Bu₃Sn(vinyl) (210 μ L, 227 mg, 0.72 mmol) were added at rt. The reaction mixture was heated at 110 °C and stirred for 5 h [progress of the reaction was monitored by TLC (hexane)]. Volatiles were evaporated and the residue was column chromatographed (5 \rightarrow 10% EtOAc/hexane) to give **B**^{9,10} (86 mg, 52%) as a light yellow powder: ¹H NMR (400 MHz, CDCl₃) δ 5.60 (dd, *J* = 10.8, 1.2 Hz, 1H), 6.13 (dd, *J* = 17.2, 1.2 Hz, 1H), 7.36 (ddd, *J* = 17.6, 10.8, 1.2 Hz, 1H), 7.74–7.88 (m, 8H), 8.08 (d, *J* = 8.8 Hz, 1H); ¹³C NMR (101 MHz, CDCl₃) δ 118.24, 122.21, 124.46, 125.66, 127.01, 127.10, 127.17, 127.22, 127.37, 127.43, 127.57, 129.05, 130.79, 130.89, 130.94, 131.05, 134.81, 134.83, 135.54, 135.64, 135.79, 136.02, 136.35, 137.88.

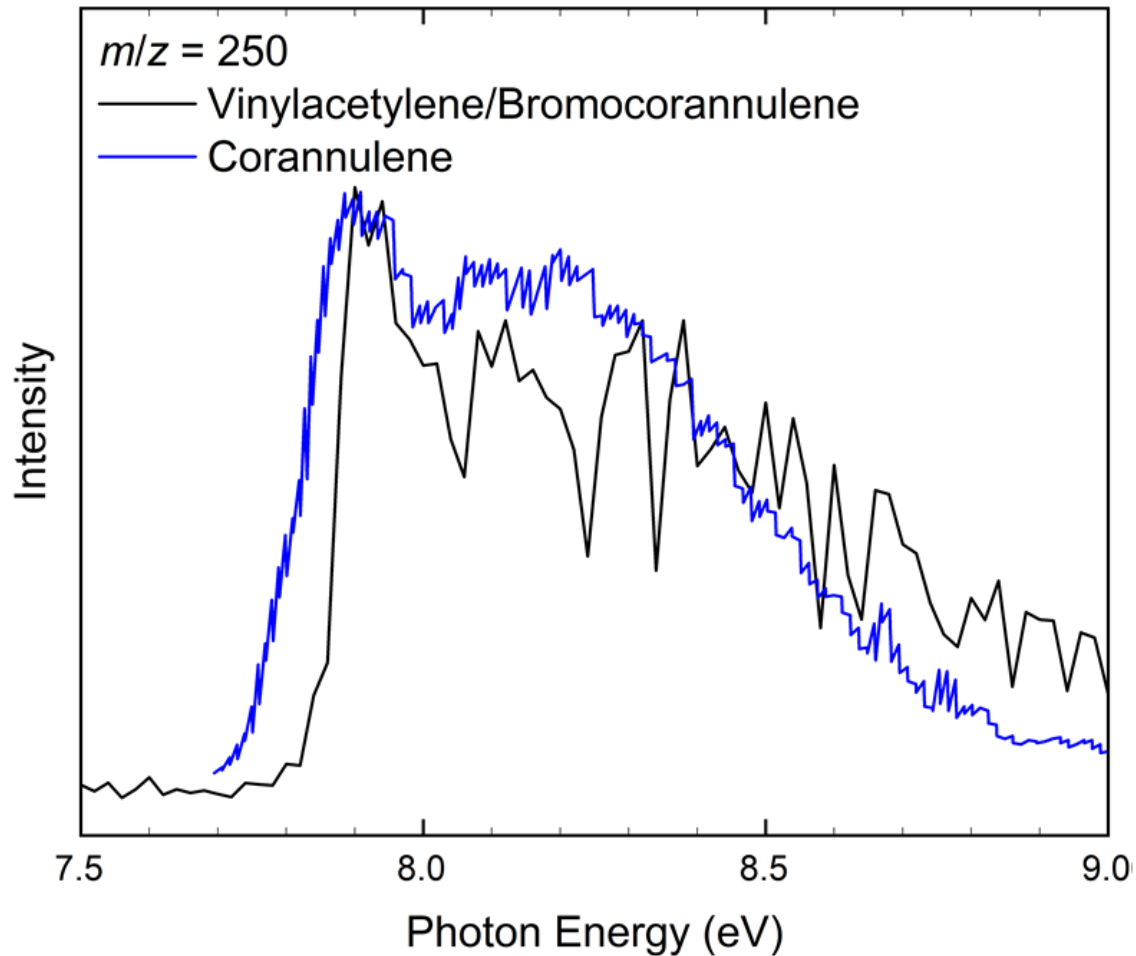
Benzocorannulene (C). Compound **B** (80 mg, 0.29 mmol) was dissolved in mixture of o-dichlorobenzene (15 mL) and nitroethanol (1.0 mL, 1.27 g, 13.9 mmol) in a pressurized flask. Phthalic anhydride (2.1 g, 14.2 mmol) was added at rt. The reaction mixture was heated at 180 °C and stirred for 3 days. Volatiles were evaporated and the residue was extracted with EtOAc. The organic layer washed with 1. 0 M NaOH (aq), brine, and anhydrous Na₂SO₄. Volatiles were evaporated and the residue was column chromatographed (5 \rightarrow 10% EtOAc/hexane) to give **C**^{11–13} (24.4 mg, 28%) as a light yellow powder: ¹H NMR (400 MHz, CDCl₃) δ 7.75 (dd, *J* = 6.0, 3.2 Hz, 1H), 7.81–7.87 (m, 2H), 7.95 (d, *J* = 8.8 Hz, 1H), 8.25 (d, *J* = 8.8 Hz, 1H), 8.67 (dd, *J* = 6.0, 3.2 Hz, 1H); ¹³C NMR (101 MHz, CDCl₃) δ 124.41, 125.22, 127.10, 127.28, 127.46, 127.68, 129.00, 130.61, 130.89, 133.29, 134.76, 135.55, 137.75.



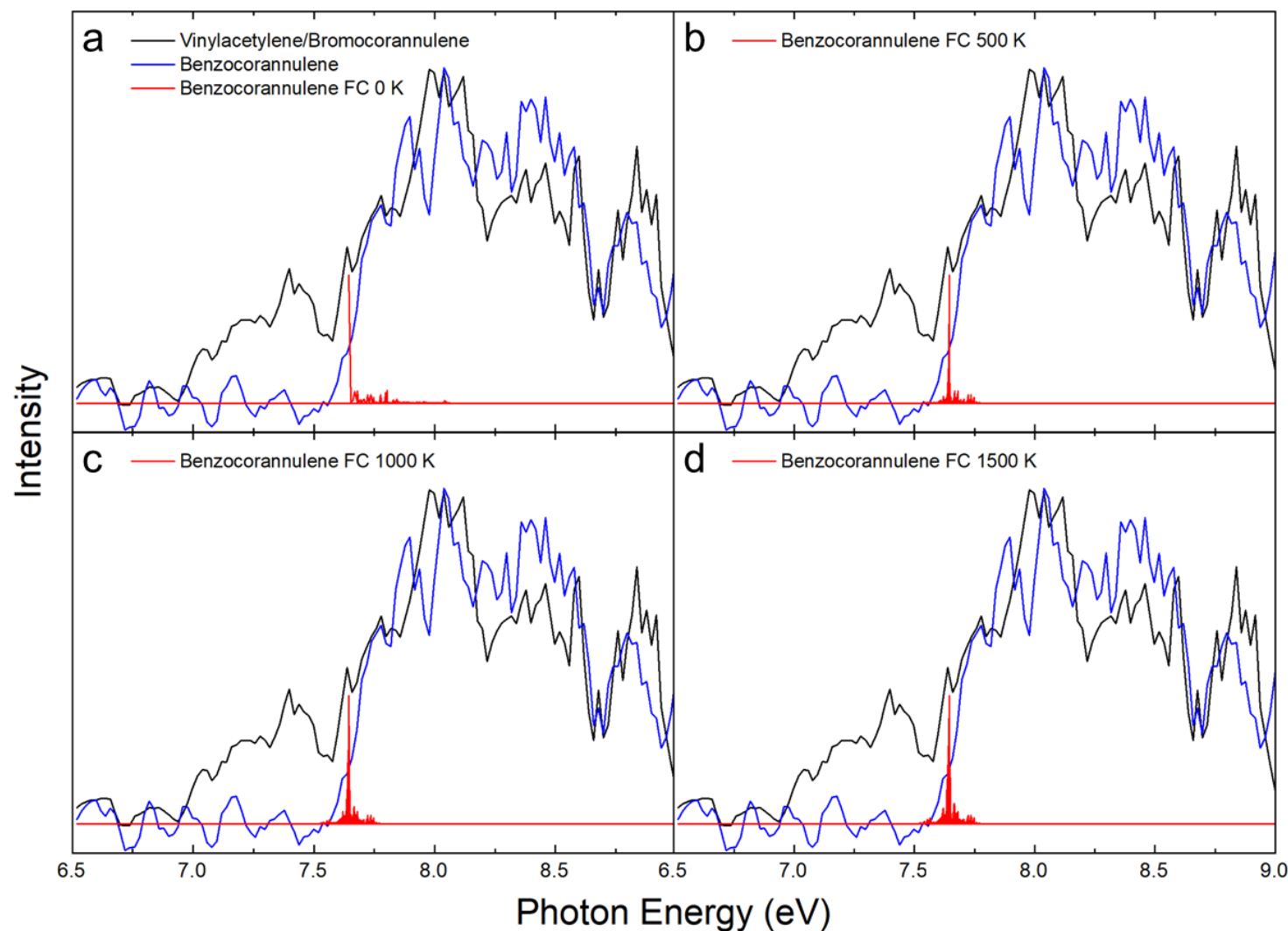
Supplementary Fig. 2 Photoionization efficiency (PIE) curves for benzocorannulene. PIE curves relevant to the formation of benzocorannulene at $m/z = 300$ ($\text{C}_{24}\text{H}_{12}$) and $m/z = 301$ ($^{13}\text{CC}_{23}\text{H}_{12}$). Black: experimentally derived PIE curve; purple: ^{13}C -substituted experimental PIE curve. The overall error bars ($m/z = 300$: gray area; $m/z = 301$: red area) consist of two parts: 1σ error of the PIE curve averaged over the individual scans and $\pm 10\%$ based on the accuracy of the photodiode.



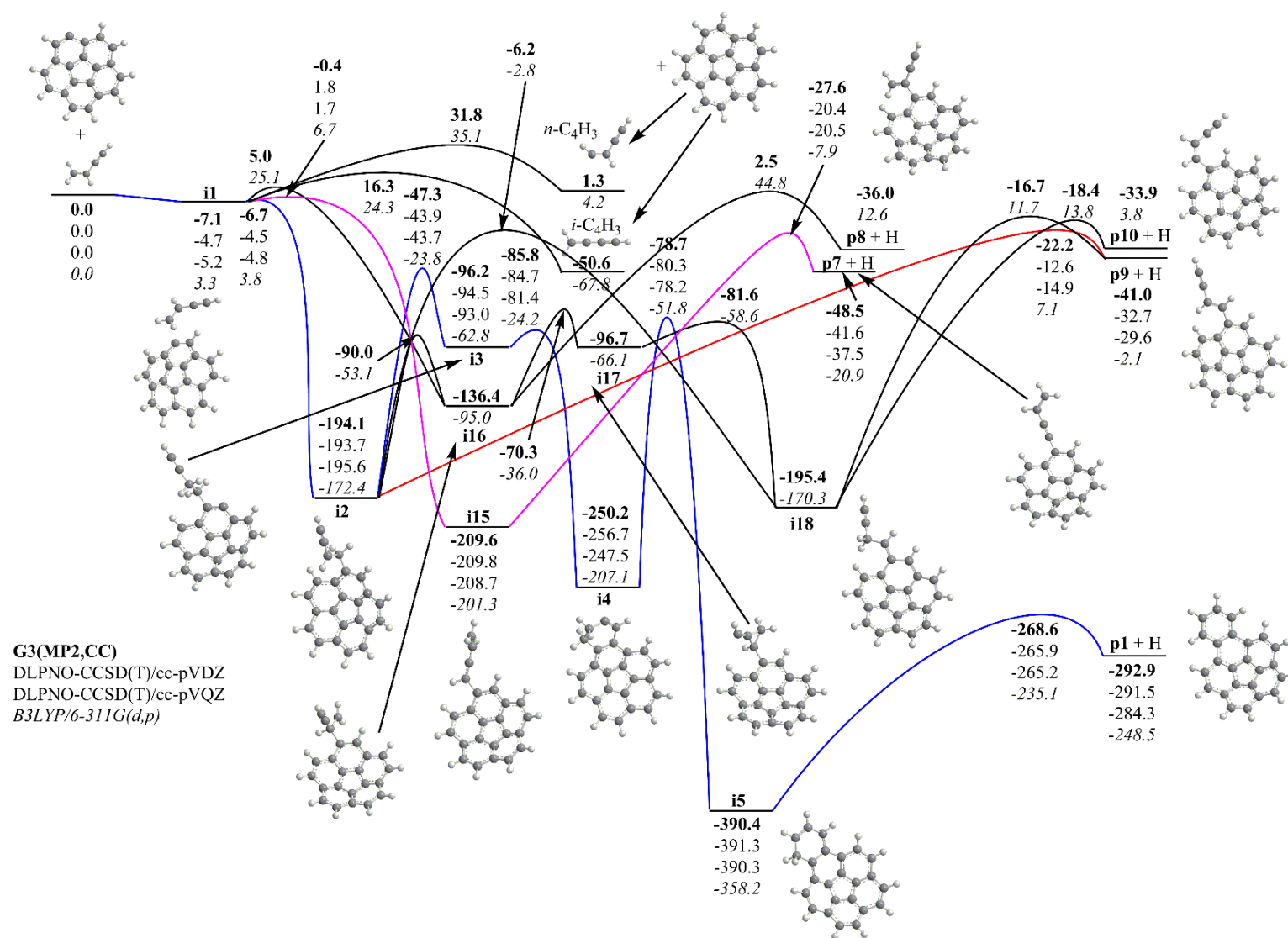
Supplementary Fig. 3 Photoionization efficiency (PIE) curves for other species. PIE curves for the vinylacetylene/bromocorannulene system at (a) $m/z = 274$ ($C_{22}H_{10}$), (b) $m/z = 328$ ($C_{20}H_9^{79}Br$), and (c) $m/z = 330$ ($C_{20}H_9^{81}Br$). The overall error bars (gray area) consist of two parts: 1σ error of the PIE curve averaged over the individual scans and $\pm 10\%$ based on the accuracy of the photodiode.



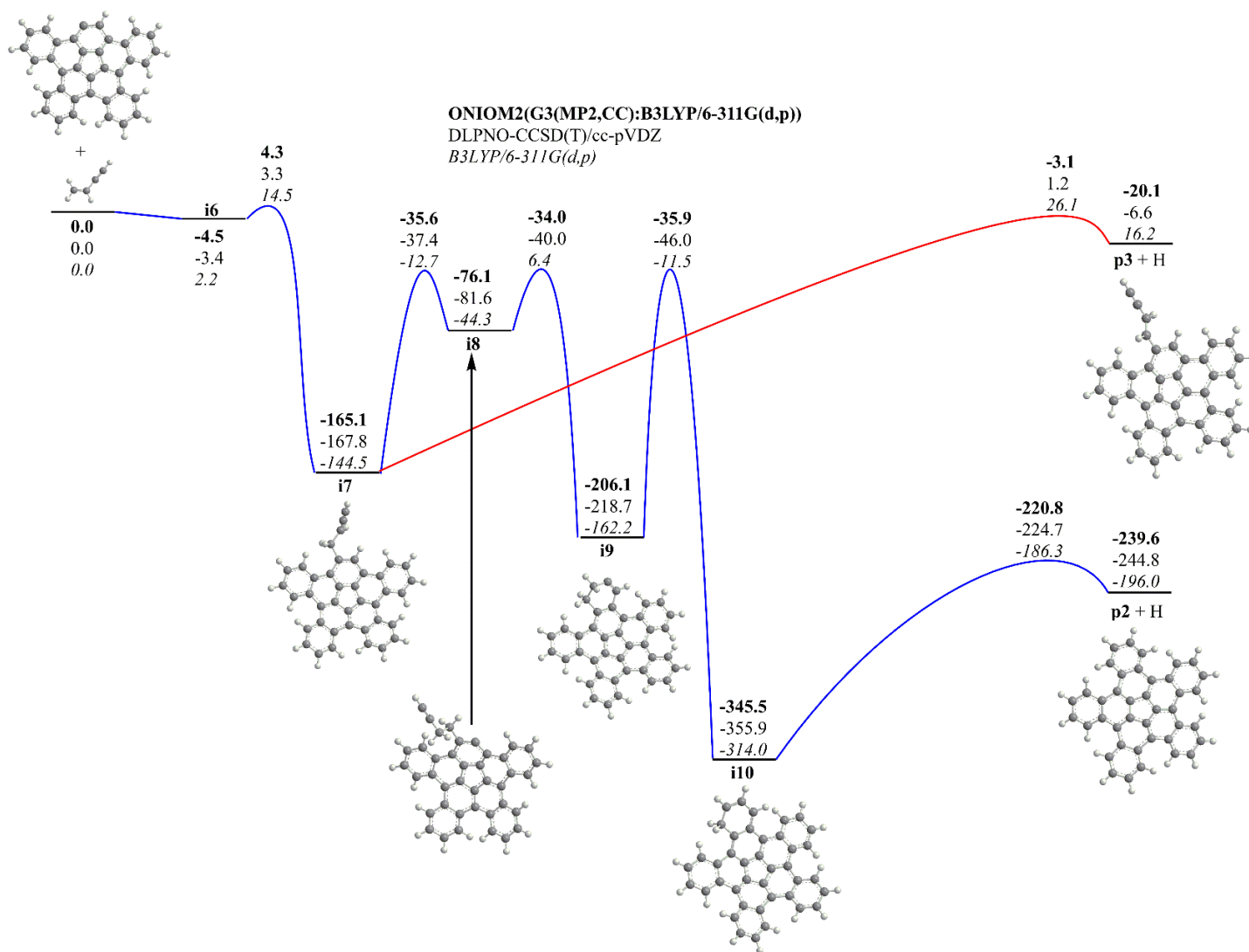
Supplementary Fig. 4 Mass-selected threshold photoelectron (ms-TPE) spectra for corannulene. (Black) ms-TPE spectrum for the vinylacetylene/bromocorannulene system at $m/z = 250$ ($C_{20}H_{10}$), and (blue) reference photoelectron spectrum of corannulene ($C_{20}H_{10}$) measured by Seiders et al¹⁴.



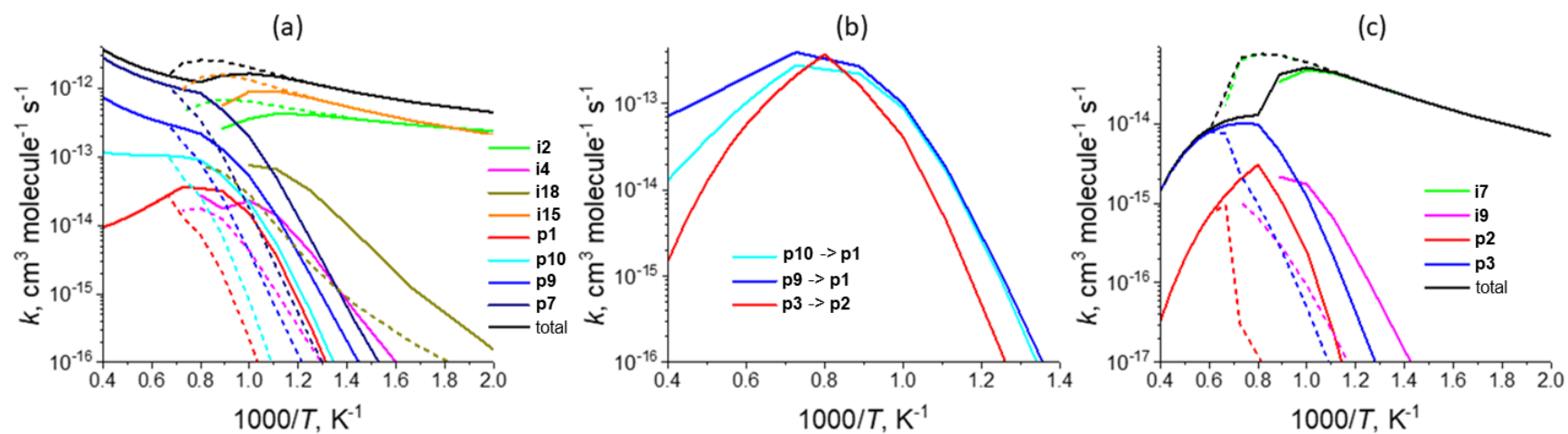
Supplementary Fig. 5 Mass-selected threshold photoelectron (ms-TPE) spectra for benzocorannulene. ms-TPE spectra relevant to the formation of benzocorannulene at $m/z = 300$ ($C_{24}H_{12}$). Black: experimentally derived ms-TPE spectrum; blue: benzocorannulene ms-TPE spectrum; red: Franck-Condon (FC) simulations for benzocorannulene at (a) 0 K, (b) 500 K, (c) 1000 K, and (d) 1500 K.



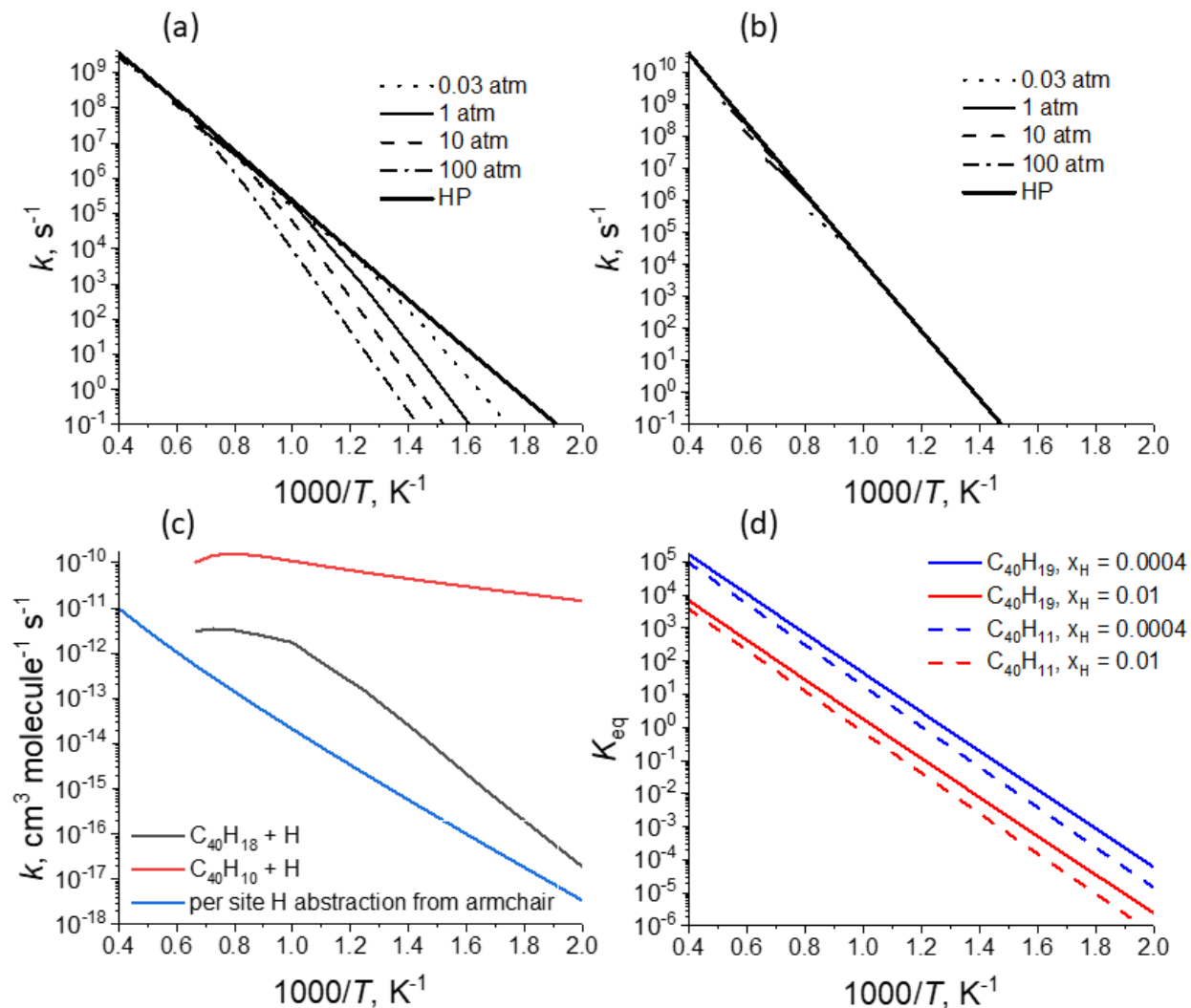
Supplementary Fig. 6 Full potential energy diagram leading to benzocorrannulene. Calculated potential energy diagram for the [C₂₀H₉]⁺ plus vinylacetylene reaction. Relative energies of various species are given in kJ mol⁻¹ with respect to the initial reactants. Carbon atoms are grey and hydrogen atoms are white.



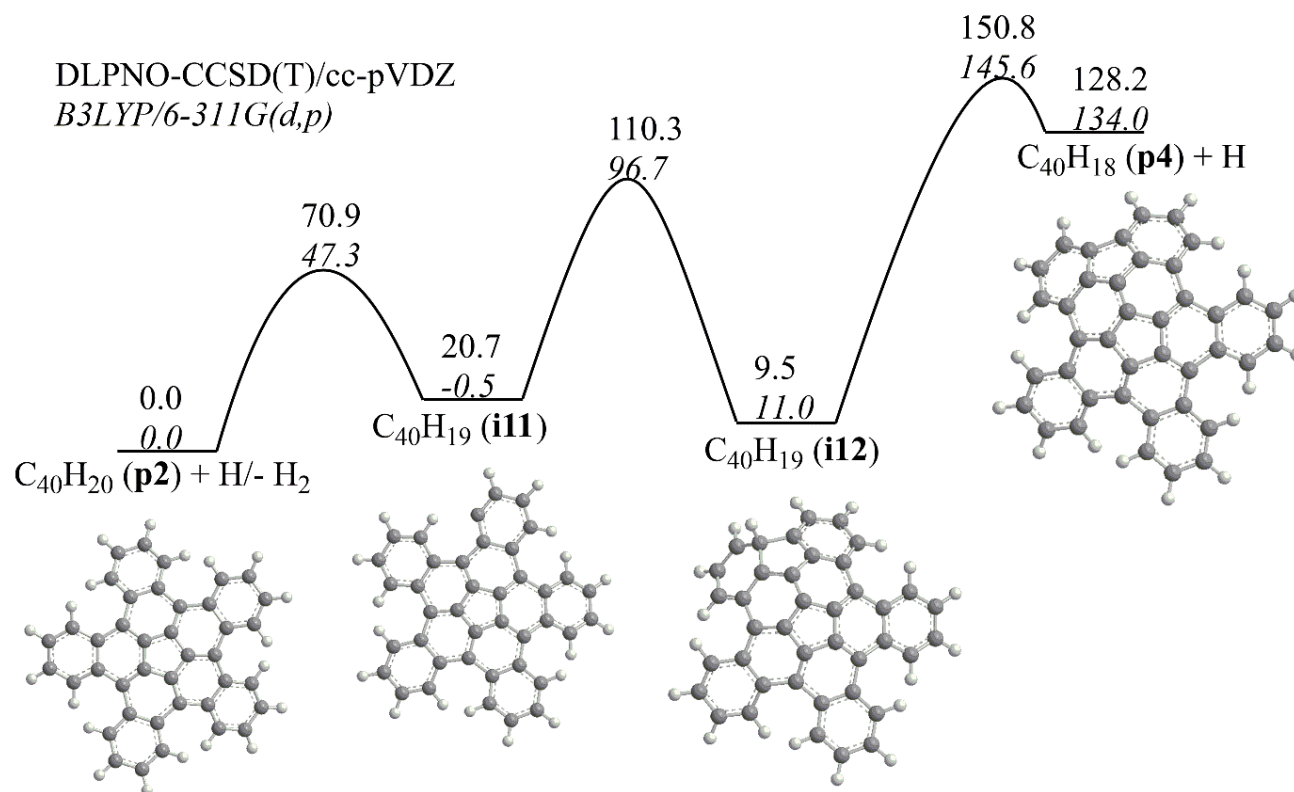
Supplementary Fig. 7 Full potential energy diagram leading to pentabenzocorannulene. Calculated potential energy diagram for the most important channels of the $[C_{36}H_{17}]^+$ plus vinylacetylene reaction. Relative energies of various species are given in kJ mol^{-1} with respect to the initial reactants. Carbon atoms are grey and hydrogen atoms are white.



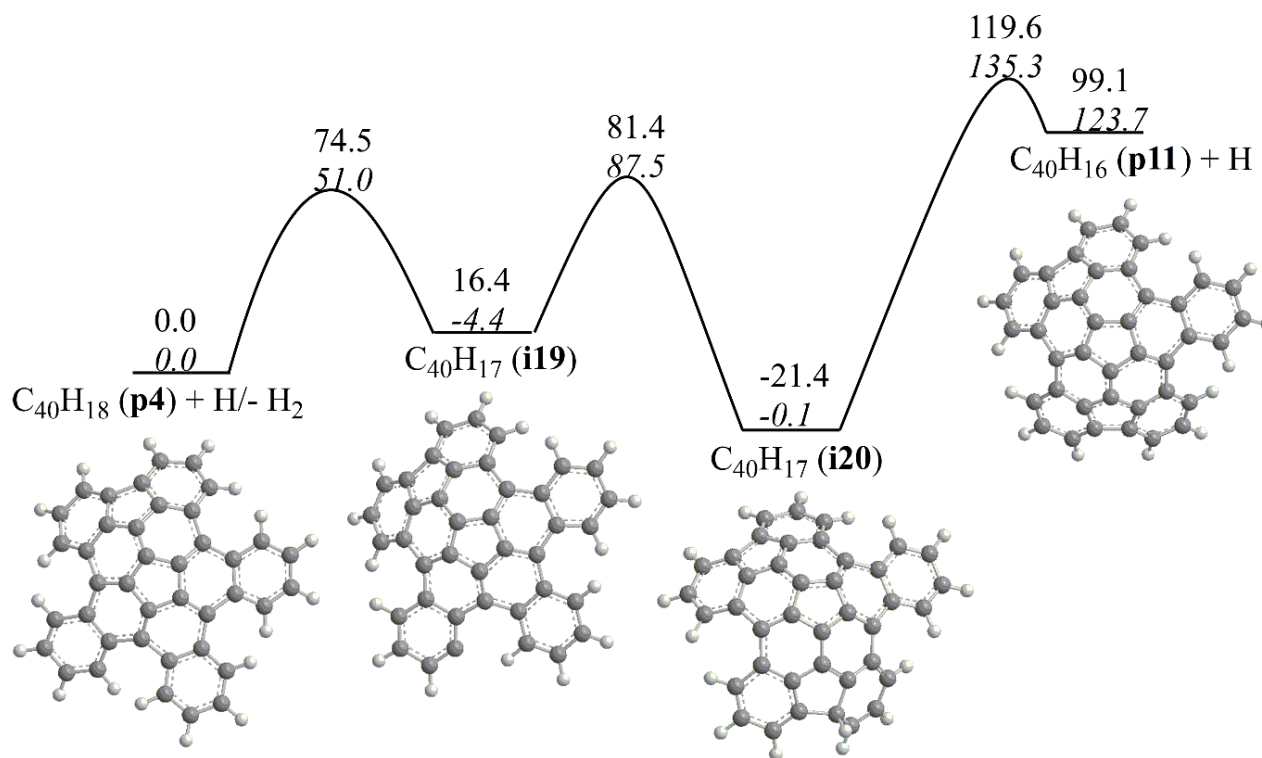
Supplementary Fig. 8 Reaction rate constants. Calculated total and individual channel rate constants for the $[\text{C}_{20}\text{H}_9]^+$ plus C_4H_4 reaction (a), for reverse reactions of hydrogen assisted isomerization of the **p10** and **p9** products to **p1** and of **p3** to pentabenzocorannulene **p2** (b), and for the $[\text{C}_{36}\text{H}_{17}]^+$ plus C_4H_4 reaction (c). Solid and dashed lines show rate constants computed at 0.03 and 1 atm, respectively.



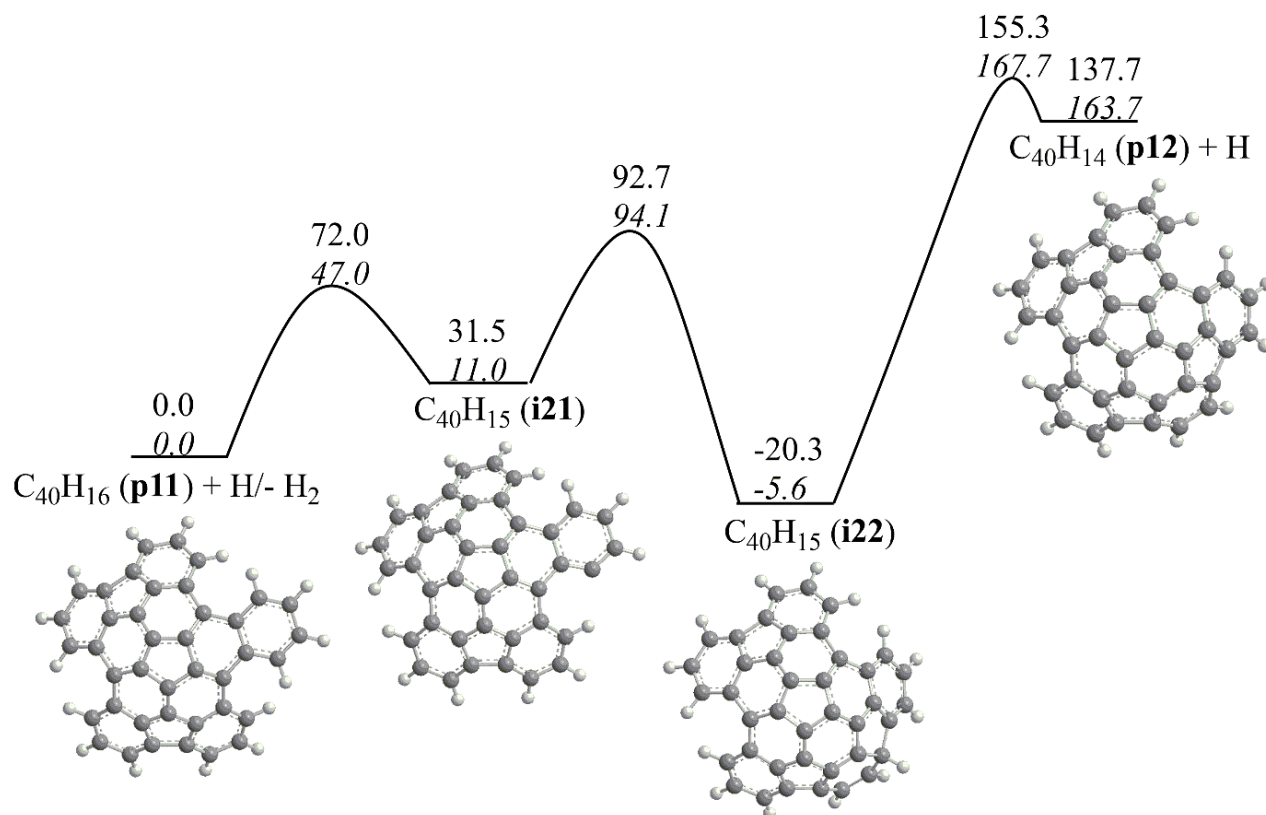
Supplementary Fig. 9 Unimolecular decomposition rate constants. Calculated rate constants for unimolecular decomposition of (a) **i11**, (b) **i14**, (c) the reverse $C_{40}H_{18}/C_{40}H_{10} + H$ addition reactions at 1 atm in comparison with a recommended per site H abstraction rate constant from a PAH armchair edge³ (d) equilibrium constants $[C_{40}H_{19}]^* \rightleftharpoons C_{40}H_{18} + H$ and $[C_{40}H_{11}]^* \rightleftharpoons C_{40}H_{10} + H$ computed at various mole fractions x_H of hydrogen atoms.



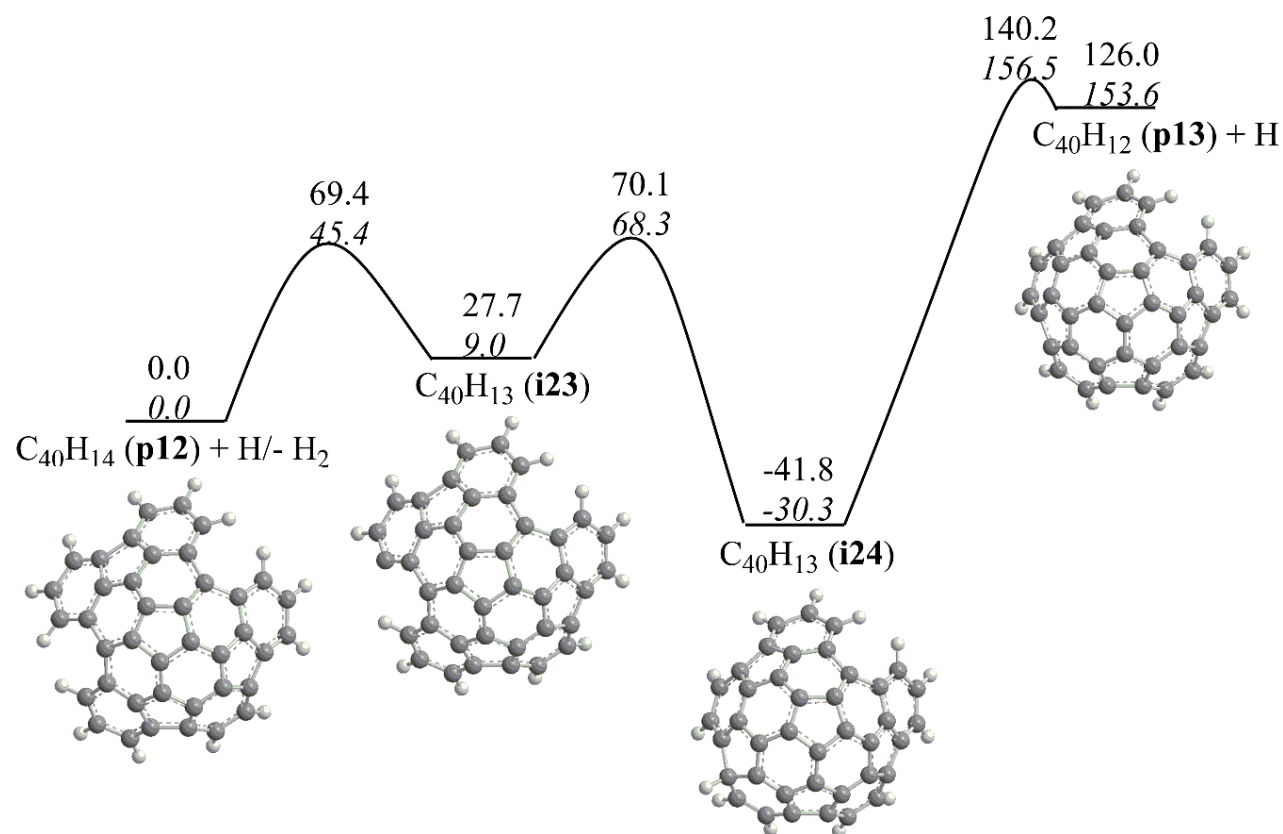
Supplementary Fig. 10a First cyclodehydrogenation step to the C40 nanobowl. Calculated potential energy diagrams for the first step in the conversion of pentabenzocorannulene ($C_{40}H_{20}$) to the C40 nanobowl ($C_{40}H_{10}$) via a sequence of five hydrogen abstraction – cyclodehydrogenation mechanisms. Relative energies of various species are given in kJ mol^{-1} with respect to the initial reactants for reaction in the sequence. Carbon atoms are grey and hydrogen atoms are white.



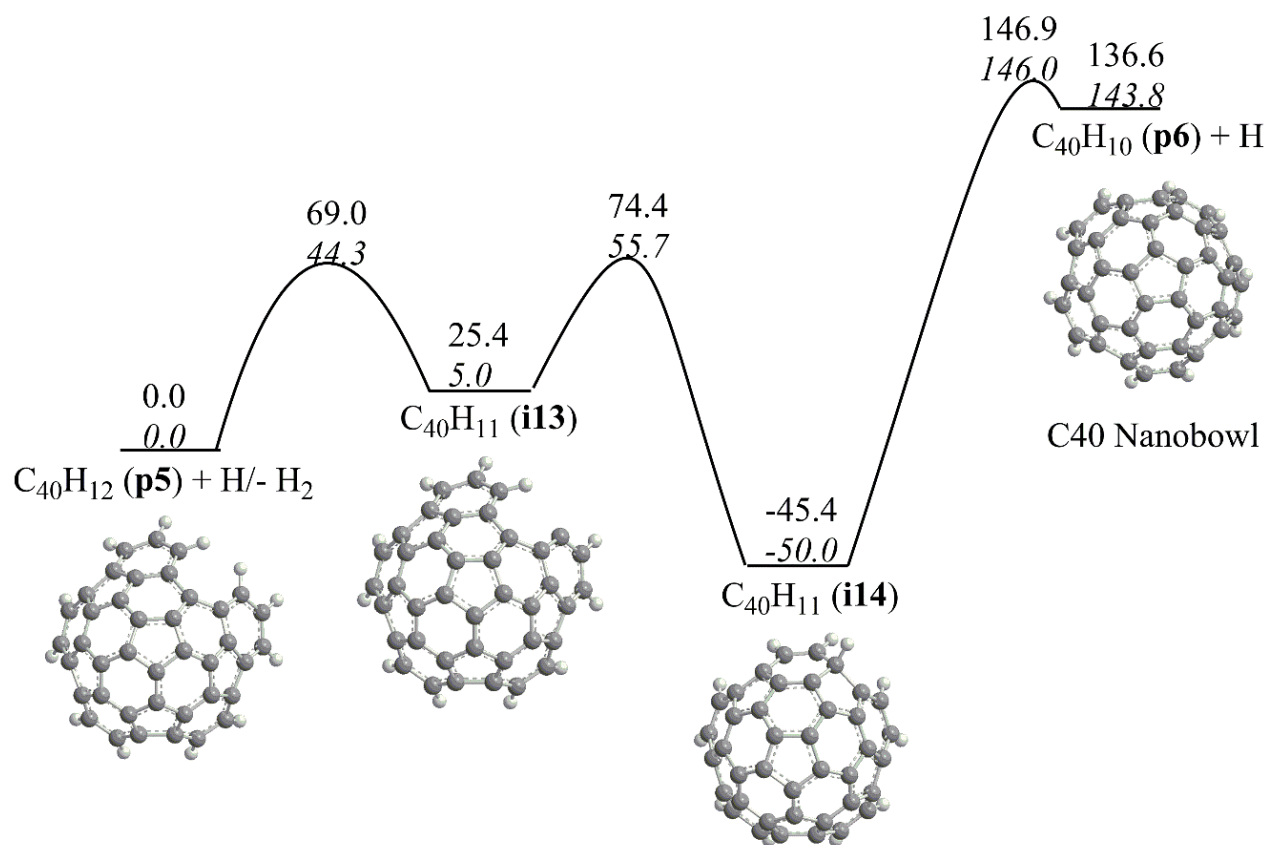
Supplementary Fig. 10b Second cyclodehydrogenation step to the C40 nanobowl. Calculated potential energy diagrams for the second step in the conversion of pentabenzocorannulene ($C_{40}H_{20}$) to the C40 nanobowl ($C_{40}H_{10}$) via a sequence of five hydrogen abstraction – cyclodehydrogenation mechanisms. Relative energies of various species are given in kJ mol⁻¹ with respect to the initial reactants for reaction in the sequence. Carbon atoms are grey and hydrogen atoms are white.



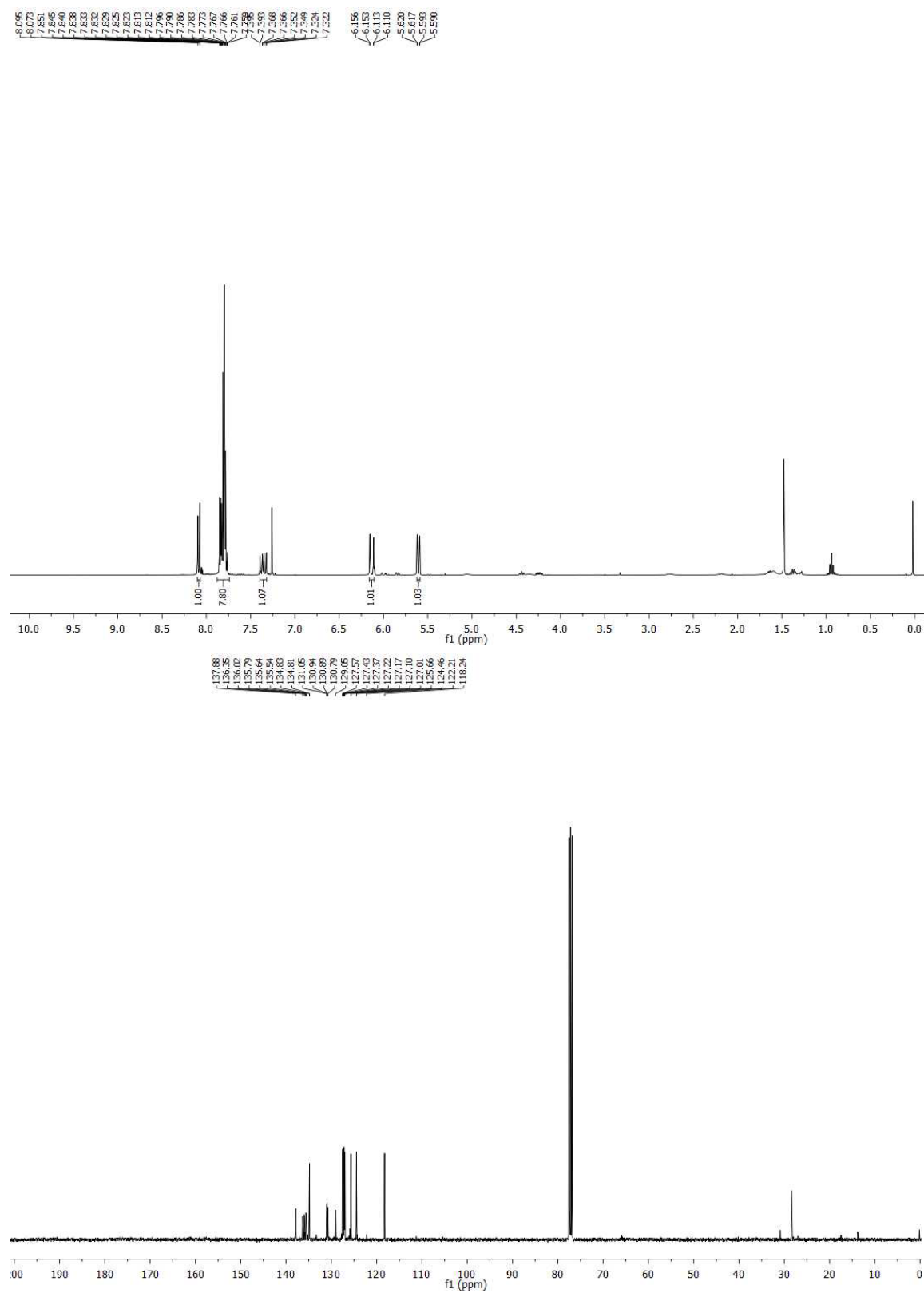
Supplementary Fig. 10c Third cyclodehydrogenation step to the C40 nanobowl. Calculated potential energy diagrams for the third step in the conversion of pentabenzocorannulene ($C_{40}H_{20}$) to the C40 nanobowl ($C_{40}H_{10}$) via a sequence of five hydrogen abstraction – cyclodehydrogenation mechanisms. Relative energies of various species are given in kJ mol^{-1} with respect to the initial reactants for reaction in the sequence. Carbon atoms are grey and hydrogen atoms are white.



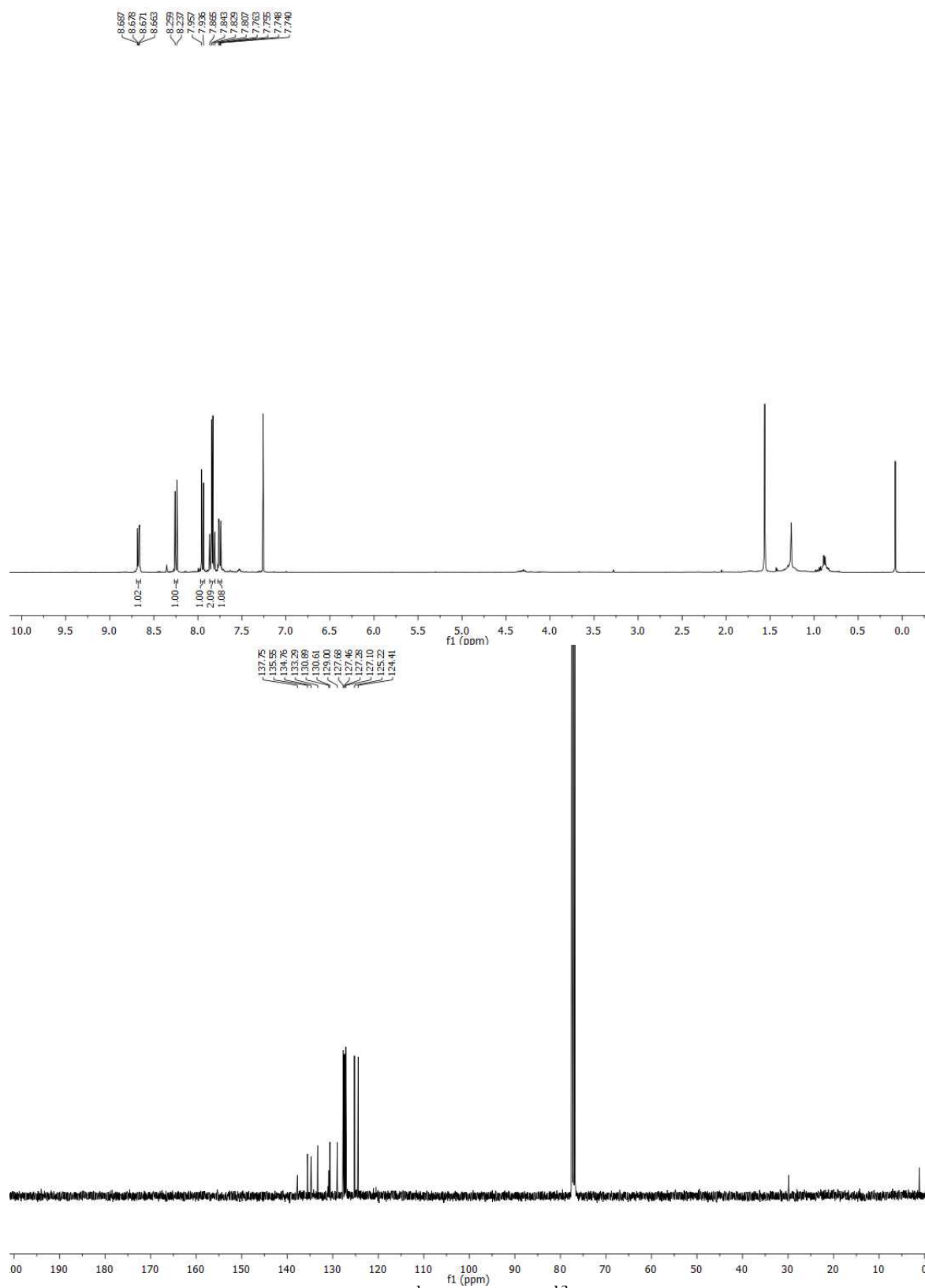
Supplementary Fig. 10d Fourth cyclodehydrogenation step to the C40 nanobowl. Calculated potential energy diagrams for the fourth step in the conversion of pentabenzocorannulene ($C_{40}H_{20}$) to the C40 nanobowl ($C_{40}H_{10}$) via a sequence of five hydrogen abstraction – cyclodehydrogenation mechanisms. Relative energies of various species are given in kJ mol⁻¹ with respect to the initial reactants for reaction in the sequence. Carbon atoms are grey and hydrogen atoms are white.



Supplementary Fig. 10e Fifth cyclodehydrogenation step to the C40 nanobowl. Calculated potential energy diagrams for the fifth step in the conversion of pentabenzocorannulene ($C_{40}H_{20}$) to the C40 nanobowl ($C_{40}H_{10}$) via a sequence of five hydrogen abstraction – cyclodehydrogenation mechanisms. Relative energies of various species are given in kJ mol⁻¹ with respect to the initial reactants for reaction in the sequence. Carbon atoms are grey and hydrogen atoms are white.



Supplementary Fig. 11 NMR spectra. ¹H NMR and ¹³C NMR spectra of compound **B** in CDCl₃.



Supplementary Fig. 12 NMR spectra. ¹H NMR and ¹³C NMR spectra of compound **C** in CDCl₃.

Supplementary Table 1. Relative energies (kJ mol⁻¹) of intermediates, transition states, and products in the reactions of phenyl and various PAH radicals with vinylacetylene.

	phenyl ^a	1-naphthyl ^b	2-tetracenyl ^c	4-phenanthrenyl ^d	corannulenyl ^e	tetrabenzo-corannulenyl ^f
i1	-17	-11	-9	-8	-7.1 (-4.7, -5.2)	-4.5 (-3.4)
i1-i2	-0.4	-2	-5	6	-6.7 (-4.5, -4.8)	4.3 (3.3)
i2	-187	-193	-195	-162	-194 (-194, -196)	-165 (-168)
i2-i3	-33	-38	-39/-42	-21	-47 (-44, -44)	-36 (-37)
i3	-91	-91	-99/-97	-62	-96 (-95, -93)	-76 (-82)
i3-i4	-58	-51	-67/-63	-26	-86 (-85, -81)	-34 (-40)
i4	-248	-244	-261/-250	-173	-250 (-257, -248)	-206 (-219)
i4-i5	-71	-56	-82/-78	-41	-79 (-80, -78)	-36 (-46)
i5	-375	-380	-386/-386	-352	-390 (-391, -390)	-346 (-356)
i5-p1	-241	-253	-229/-264	-224	-269 (-266, -265)	-221 (-225)
p1 + H	-265	-277	-243/-285	-246	-293 (-292, -284)	-240 (-245)
i2-p9	-21	-16	-24	8	-22 (-13, -15)	-3 (-1)
p9 + H	-36	-29	-38	-15	-41 (-33, -30)	-20 (-7)
i1-i15	5	3	3	9	-0.4 (1.8, 1.7)	
i15	-208	-202	-212	-179	-210 (-210, -209)	
i15-p7	-22	-25	-27	-6	-28 (-20, -21)	
p7 + H	-42	-49	-46	-28	-49 (-42, -38)	

^aFrom¹. The ring annulation product is naphthalene.

^bFrom². The ring annulation product is phenanthrene.

^cFrom³. For the species along the ring annulation pathways, the first number corresponds to the channel leading to the formation of pentacene and the second number corresponds to the channel leading to benzo[a]tetracene.

^dFrom⁴. The ring annulation product is [4]-helicene.

^eThe ring annulation product is benzocorannulene. For each species, the first number is calculated at the G3(MP2,CC) level of theory and the numbers in parentheses are obtained at the DLPNO-CCSD(T) level with the cc-pVDZ (italic) and cc-pVQZ basis sets.

^fThe ring annulation product is pentabenzocorannulene. For each species, the first number is calculated at the ONIOM2{G3(MP2,CC):B3LYP/6-311G(d,p)} level of theory and the number in parentheses (italic) is obtained at the DLPNO-CCSD(T)/cc-pVDZ level.

Supplementary References

1. Zhao, L. et al. A VUV photoionization study on the formation of the simplest polycyclic aromatic hydrocarbon: naphthalene ($C_{10}H_8$). *J. Phys. Chem. Lett.* **9**, 2620-2626 (2018).
2. Zhao, L. et al. Low-temperature formation of polycyclic aromatic hydrocarbons in Titan's atmosphere. *Nat. Astron.* **2**, 973-979 (2018).
3. Zhao, L. et al. A free radical prompted barrierless gas phase synthesis of pentacene. *Angew. Chem., Int. Ed.* **59**, 11334-11338 (2020).
4. Zhao, L. et al. Gas phase synthesis of [4]-helicene. *Nat. Comm.* **10**, 1510 (2019).
5. Semenikhin, A. S. et al. Rate constants for H abstraction from benzo(a)pyrene and chrysene: a theoretical study. *Phys. Chem. Chem. Phys.* **19**, 25401-25413 (2017).
6. Frenklach, M. & Mebel, A. M. On the mechanism of soot nucleation. *Phys. Chem. Chem. Phys.* **22**, 5314-5331 (2020).
7. Frenklach, M., Semenikhin, A. S. & Mebel, A. M. On the mechanism of soot nucleation. III. the fate and facility of the E-bridge. *J. Phys. Chem. A* **125**, 6789-6795 (2021).
8. Xu, B., Guo, T. & Siegel, J. Mono- and *sym*-pentahalogenated corannulenes: reaction optimization & purification by in process product analysis. *React. Chem. Eng.* **7**, 1230-1235 (2022).
9. Mack, J., Vogel, P., Jones, D., Kaval, N. & Sutton, A. The development of corannulene-based blue emitters. *Org. Biomol. Chem.* **5**, 2448-2452 (2007).
10. Muzammil, E. M., Halilovic, D. & Stuparu, M. C. Synthesis of corannulene-based nanographenes. *Comm. Chem.* **2**, 58 (2019).
11. Smith, N. J. Ph.D dissertation, Boston College. Graduate School of Arts and Sciences (2011).
12. Rajeshkumar, V., Lee, Y. T. & Stuparu, M. C. Corannulenecarbaldehyde: high-yielding synthesis by Rieche formylation and facile access to a variety of corannulene derivatives. *Eur. J. Org. Chem.* **2016**, 36-40 (2016).
13. Peng, L. & Scott, L. T. Interconversions of aryl radicals by 1,4-shifts of hydrogen atoms. a synthesis of benzo[a]corannulene. *J. Am. Chem. Soc.* **127**, 16518-16521 (2005).
14. Seiders, T. J., Baldrige, K. K., Siegel, J. S. & Gleiter, R. Ionization of corannulene and 1,6-dimethylcorannulene: photoelectron spectra, electrochemistry, charge transfer bands and ab initio computations. *Tetrahedron Lett.* **41**, 4519-4522 (2000).